TIMING VAPOR–MELT EQUILIBRATION IN SILICIC MAGMAS

by

MADISON MITCHELL BALL

A THESIS

Presented to the Department of Earth Sciences
and the Graduate School of the University of Oregon
in partial fulfillment of the requirements
for the degree of
Master of Science

June 2017

THESIS APPROVAL PAGE

Student: Madison Mitchell Ball

Title: Timing Vapor–Melt Equilibration in Silicic Magmas

This thesis has been accepted and approved in partial fulfillment of the requirements for the Master of Science degree in the Department of Earth Sciences by:

James Watkins	Chairperson
Paul Wallace	Member
Thomas Giachetti	Member

and

Scott L. Pratt	Dean of the Graduate School

Original approval signatures are on file with the University of Oregon Graduate School.

Degree awarded June 2017

THESIS ABSTRACT

Madison Mitchell Ball

Master of Science

Department of Earth Sciences

June 2017

Title: Timing Vapor–Melt Equilibration in Silicic Magmas

Magmas experiencing pressure changes can follow equilibrium or nonequilibrium degassing paths that determine the rate of gas exsolution and the composition of gases exsolved. Many variables influence timescales of equilibration between vapor and melt after a perturbation in pressure, temperature, or other factors, and the magnitude of this equilibration time determines whether the system experiences equilibrium degassing or not. In order to create a simplified framework for assessing degassing regime, we constructed a numerical diffusion model to test the sensitivity of equilibration time to variables such as bubble size, spacing, melt temperature, initial and final system pressures, and water content. We then determined the degassing regime for a range of bubble-spacing and decompression rates as an initial simplified framework to build on. We also attempted the first mixed-volatile continuous decompression experiments in order validate our model and further improve analyses and interpretations of volatile gradients in natural samples.

CURRICULUM VITAE

NAME OF AUTHOR: Madison Mitchell Ball

GRADUATE AND UNDERGRADUATE SCHOOLS ATTENDED:

University of Oregon, Eugene
University of Chicago, Chicago

DEGREES AWARDED:

Master of Science, Geological Sciences, 2017, University of Oregon
Bachelor of Science, Geophysical Sciences, 2015, University of Chicago

AREAS OF SPECIAL INTEREST:

Geochemistry
Volcanology
Paleoclimatology

PROFESSIONAL EXPERIENCE:

Graduate Employee, University of Oregon, 2015-2017

ACKNOWLEDGMENTS

First, I'd like to thank the supportive and wonderful community of graduate students, staff, post-docs, and professors that is the Department of Earth Sciences at the University of Oregon. I'd especially like to thank my advisor—James Watkins—my thoughtful committee members—Paul Wallace and Thomas Giachetti—and our wonderful office staff—Marla, Sandy, and Dave—without whom, the department would grind to a halt. I'd also like to express my gratitude to Madison Myers, an inspiring scientist and friend, as well as Marisa Acosta, Erin Hoxsie, Mike Hudak, and Win McLaughlin along with many others for always providing bright spots in my days here.

Without the continual support and love of my wonderful parents, I wouldn't be anywhere close to where I am today, and I'll never be able to properly express my appreciation for everything they've done for me. I'd also like to thank Julia and Watson for always keeping me focused on what's important and staying by my side. I'm also grateful to Danielle Labotka for consistent cross-country grad school commiseration.

Lastly, thank you to the GTFF and Department for always making sure us graduate students are well looked after. I am fortunate to have had this work funded from NSF grant EAR-1249404 awarded to James Watkins.

TABLE OF CONTENTS

Chapter	Page
I. INTRODUCTION AND BACKGROUND	1
An Introduction to Volcanic Conduits	1
Volatile Solubility in Silicic Melts	2
Bubble Formation and Growth	5
Degassing Paths	8
Observations of Non-Equilibrium Degassing	10
Research Questions	10
II. METHODS	12
Capsule Assembly	12
The Rapid Quench Cold Seal Pressure Vessel	14
Sample Preparation for FTIR Analysis	15
III. QUANTITATIVE ANALYSIS OF VOLATILES IN SILICATE GLASS USING FOURIER TRANSFORM INFRARED SPECTROSCOPY	17
Introduction	17
The Advantages of FTIR	18
Spectroscopy	18
How the FTIR Works	21
Quantitative Analysis	27
IV. STEP-DECOMPRESSION MODELING, RESULTS, AND DISCUSSION	30
Step-Decompression Model Methods	30
Step-Decompression Modeling Results	34

Chapter Page

Continuous-Decompression Modeling Results 37

Discussion 38

V. EXPERIMENTAL RESULTS AND DISCUSSION 43

Solubility Experiment Results 43

Mixed Volatile Decompression Experiment Results 46

H_2O Only Experiment Results 49

Discussion of Experimental Results 50

VI. CONCLUSION 56

APPENDICES 58

A. TABLE OF EXPERIMENTS PERFORMED 58

B. SHARDS OF FIRE 59

REFERENCES CITED 62

LIST OF FIGURES

Figure Page

1.1. Solubility calculations for pure H_2O vs. pressure and pure CO_2 vs. pressure 4

1.2. Solubility calculations for H_2O–CO_2 volatile mixture dissolved in rhyolite 5

1.3. Different models showing late-stage, low-pressure degassing paths of H_2O and CO_2 in the far-field melt 9

2.1. Photographs of capsule assembly components 13

2.2. Schematic of a nearly-complete assembled capsule with all components 14

2.2. Schematic of a nearly-complete assembled capsule with all components 14

3.1. Schematic example of a broadband blackbody spectrum 19

3.2. Illustration of the vibrational modes of molecular H_2O, OH, and CO_2 21

3.3. Light path through the FTIR spectrometer 22

3.4. A simplified interferogram is constructed from waves of different wavelength and amplitude 25

4.1. Schematic illustration of two different model runs 31

4.2. Evolution of the far-field melt CO_2 concentration after instantaneous decompression 33

4.3. Results of calculating equilibration timescales of bubbles varying 1-1000 μm in radius with spacing ranging from 50-500 μm after a pressure drop 34

4.4. Equilibration time plotted against temperature of model run 35

4.5. Equilibration time plotted against pressure-drop magnitude of model run 36

4.6. Equilibration time plotted against initial pressure of model run 36

4.7. Equilibration time plotted against mole-fraction H_2O of model run 37

4.8. Results of continuous decompression model runs with variable decompression rate and bubble-spacing/BND 38

Figure Page

4.9. Model tested against decompression experiments of Yoshimura and Nakamura (2010a) 40

5.1. H_2O–CO_2 concentration in glass after 4, 6, and 8 days 44

5.2. Synthetic obsidian equilibrated at 800°C and 100 MPa for 25 days 45

5.3. Mono Craters obsidian equilibrated at 800°C and 100 MPa for 13 days 46

5.4. Synthetic obsidian equilibrated for 14 days and decompressed at 0.01 MPa/s 47

5.5. Synthetic obsidian equilibrated for 25 days and decompressed at 0.01 MPa/s 48

5.6. Natural obsidian equilibrated for 11 days and decompressed at 0.01 MPa/s 49

5.7. Two natural obsidian samples equilibrated for 4 days each and decompressed at 0.01 MPa/s 50

5.8. Time for CO_2 concentration in the far-field melt to reach equilibrium 54

LIST OF TABLES

Table Page

1.1. Coefficient and error values for equations (1a) and (1b) 3

2.1. Bulk composition of rhyolitic obsidian used in experiments..... 13

2.2. Masses of capsule after addition of each component..... 14

3.1. Strengths and weaknesses of common micro-analytical techniques 18

5.1. List of solubility experiments 43

5.2. List of mixed-volatile decompression experiments 46

CHAPTER I

INTRODUCTION AND BACKGROUND

Chapter 1.1
An Introduction to Volcanic Conduits

More than any other question, volcanologists seek to understand how magma comes to the surface and erupts, often with dramatic and hazardous consequences. Magma reservoirs generally form at depths 5-25 km below the surface, so the transportation of magma from depth to the surface requires an intermediary structure known as the volcanic conduit (Becerril et al., 2013; Scandone, 1995). While residing at depth in the magma chamber, the pressurized magma contains dissolved volatiles—primarily H_2O, CO_2, and SO_2. During an eruption, the magma rises through the conduit, driven by overpressurization of the magma chamber and buoyancy of the melt (Sparks, 1978). As magma rises in the conduit and depressurizes, dissolved volatiles become supersaturated in the melt as their solubility in the melt falls.

Once sufficiently supersaturated, bubbles form in the melt, and the rising magma accelerates as bubbles expand and move upwards due to buoyancy forces. In explosive eruptions, the positive feedback cycle of bubble nucleation/growth and ascent rate accelerates until the molten rock becomes an unstable foam that fragments into pyroclastic material, which can then be forcefully ejected out of the volcano in huge volumes. In effusive eruptions, the melt ascends slowly enough that volatiles are able to rise out of or create channels of escape through the melt, preventing runaway nucleation. Many variables control the behavior of ascending magma making volcanic conduits

complicated systems to study— subtle differences in melt composition, volatile content, degassing history, local and regional stress fields, previous eruption history among many other factors can make the difference between Mt. St. Helens' explosive, dangerous 1982 eruption and the effusive, non-hazardous dome-forming events since. As people largely care about volcanoes for their ability to erupt, our collective desire to understand and, hopefully, predict these eruptions necessitates the study of conduits and the complex processes that bring magma to the surface.

Chapter 1.2
Volatile Solubility in Silicic Melts

Of the factors that control solubility of dissolved volatiles in melt— temperature, pressure, melt composition, and the volatile mixture itself —pressure dominates the solubility relationship and has the most powerful control on volatile saturation states in melts of a given composition. Much like carbonation leaving a soda, when volatiles become supersaturated with respect to the equilibrium solubility (e.g. during ascent and depressurization) a separate gas phase exsolves from the fluid melt. These dissolved volatile species must first nucleate new bubbles and then be transported to existing bubbles. Liu et al. (2005) quantified empirical relationships for the coupled solubility of H_2O and CO_2 in a rhyolite melt as a function of temperature, pressure, and gas composition. These volatile species—H_2O and CO_2— will be the focus of this study. While solubility relationships for SO_2 in silicic magmas have been studied (Clemente et al., 2004; Carroll and Rutherford, 1985), the solubility behaviors of this volatile species are not well constrained in highly silicic melts (e.g. Mavrogenes and Neill, 1999).

Magma reservoir depths of 5-25 km correspond to a pressure range of ~100-600 MPa (dependent on melt density, local stress fields, and gas overpressurization). At 100 MPa and 800°C, a silicic melt can support ~4 wt. % of pure H_2O or ~530 ppm of pure CO_2 as estimated by the empirical relationship developed by Liu et al. (2005):

$$H_2O_t = \frac{a_1 P_w^{0.5} + a_2 P_w + a_3 P_w^{1.5}}{T} + a_4 P_w^{1.5} + P_{CO_2}(a_5 P_w^{0.5} + a_6 P_w) \quad (1.1a)$$

$$CO_2 = \frac{b_1 P_{CO_2}}{T} + P_{CO_2}(b_2 P_w^{0.5} + b_3 P_w^{1.5}) + \frac{b_4 P_{CO_2} P_w}{T} \quad (1.1b)$$

where H_2O_t is H_2O dissolved in the melt in wt.%, CO_2 content is in ppm dissolved in the melt by mass, P_w is mole fraction of H_2O (X_w) multiplied by P—the pressure in MPa, P_{CO2} is mole fraction of CO_2 (X_{CO2}) multiplied by P, and T is the temperature in Kelvin. The values for the constants and their associated errors are listed in Table 1.1. In a pure-H_2O system ($P_{CO2} = 0$), P_w will equal the pressure of the system (P) and vice-versa for a pure-CO_2 system. The concentration curves in Figure 1.1 demonstrate the relative insensitivity of volatile solubility to small variations in temperature compared to variations in pressure. For a pressure of 100 MPa, a temperature change from 1200 to 700°C ($\Delta T = 500°C$) increases the solubility of pure H_2O from 3.3 wt. % to 4.3 wt. % and pure CO_2 from 385 to 582 ppm. A temperature change from 800 to 700°C (($\Delta T = 100°C$)

Table 1.1. Coefficient and error values for equations (1a) and (1b).

	Eq. (1a)		Eq. (1b)	
i	a_i	Error	b_i	Error
1	354.94	4.55	5668	127
2	9.623	0.923	0.4133	0.0491
3	-1.5223	0.0722	2.041×10^{-3}	0.285×10^{-3}
4	0.0012439	0.0000499	-55.99	8.36
5	-1.084×10^{-4}	0.406×10^{-4}		

increases solubility of H_2O by 0.3 wt. % and CO_2 by 54 ppm, so in a natural system with temperatures constant within 50°C, the effect on solubility due to temperature fluctuations will be vastly subordinate to the effects due to pressure fluctuations, especially at pressures below 100 MPa.

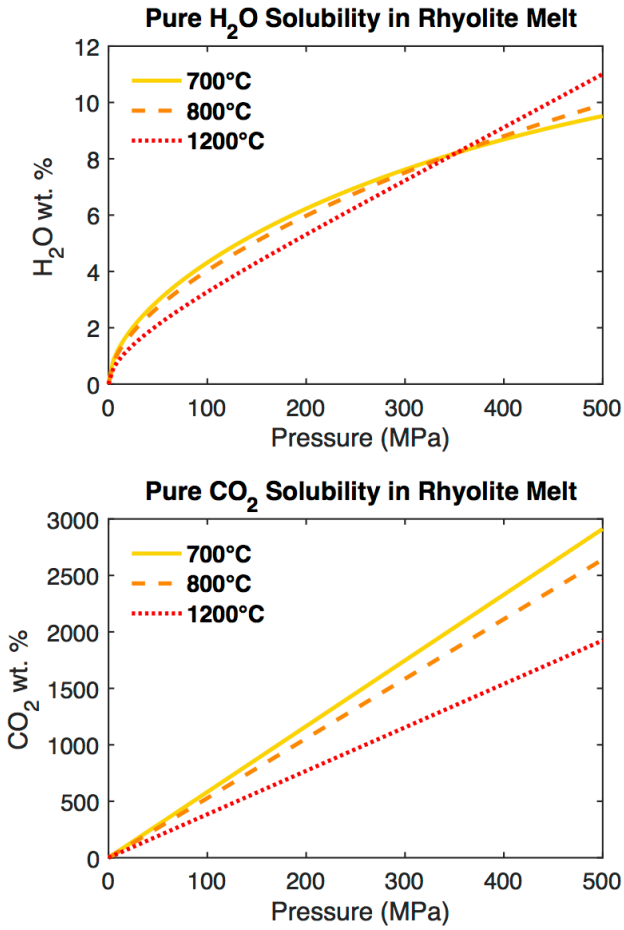

Figure 1.1. Solubility calculations for pure H_2O (0 ppm CO_2) vs. pressure and pure CO_2 (0 wt. % H_2O) vs. pressure for temperatures of 700, 800, and 1200°C. Solubility relationship from Liu et al. (2005).

In the pure-H_2O or pure-CO_2 solubility case, for a melt of constant composition, volatile saturation depends only on temperature and pressure as shown in Figure 1.1. When a melt contains multiple volatile species however, the relative abundances of each species can change the solubility of the other species in melt as seen in Figure 1.2. Melt properties such as bulk composition and polymerization limit the total content of volatiles that can remain dissolved in the melt at equilibrium for a specific temperature and pressure. If a system originates with a pure H_2O magma system and a CO_2 rich fluid begins fluxing through it, some H_2O will be forced to exsolve from the melt in order to accommodate the CO_2, as the dissolved gas content must be proportional to its partial pressure in the exsolved vapor phase.

At fixed pressures, temperatures, and melt compositions, the equilibrium solubility of a mixed volatile system depends entirely on the mole fraction of the volatile components. The arcing lines of Figure 1.2 show temperature-dependent isobars. Isobars are more useful than isotherms because of the sensitivity of solubility to pressure compared to temperature in magmatic systems. Note that the addition of a small amount of H_2O to an anhydrous system depolymerizes the melt and increases the solubility of CO_2, as the melt becomes depolymerized. Then once the melt reaches peak depolymerization, the two volatile species have an inverse solubility relationship.

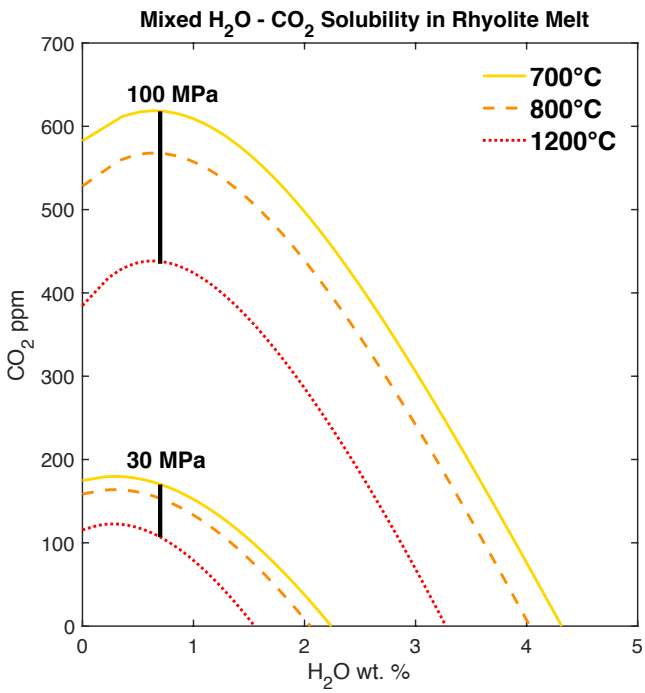

Figure 1.2.
Solubility calculations for H_2O–CO_2 volatile mixture dissolved in rhyolite melt at two pressures (30, 100 MPa) and three temperatures (700, 800, and 1200°C). Solubility relationship from Liu et al. (2005)

Chapter 1.3
Bubble Formation and Growth

When a melt that has equilibrated at depth experiences a drop in pressure, the dissolved volatiles become supersaturated in the melt. Once the critical supersaturation pressure is reached (ΔP_N, the difference between gas pressure in the melt and ambient pressure) a separate gas phase exsolves out of the melt forming bubbles (Fiege and Cichy, 2015). These bubbles can either exploit preferential nucleation sites on crystals

and other impurities in the melt (heterogeneous nucleation) or they can spontaneously nucleate throughout regions of supersaturated melt (homogeneous nucleation). Natural systems contain abundant crystals and impurities that can serve as nucleation sites, so heterogeneous nucleation—requiring relatively lower degrees of supersaturation than homogeneous nucleation— would be presumed to be the predominant mode of nucleation (Manga et al., 2004a; Fiege and Cichy). These two nucleation processes are not mutually exclusive, and as melt between crystal grains can achieve the critical supersaturation for homogeneous nucleation before the volatiles can diffuse to bubbles forming concurrently at heterogeneous nucleation sites.

As long as melt remains supersaturated with volatiles for a given set of *P–T* conditions, volatiles will continue to exsolve, either nucleating new bubbles or diffusing to and growing existing bubbles. To determine whether bubble nucleation or growth dominate a melt system, either the bubble size distribution (BSD) or the bubble number density (BND) and porosity (Φ, the volume fraction of void space compared to the bulk volume) of a melt can be measured and used. The BSD deals with the number of bubbles of a certain size per unit volume as a histogram of population density vs. bubble size. Melts that are dominated by nucleation rather than growth will show large numbers of small bubbles and few large bubbles, while growth-dominated melts will have the opposite trend with a number of large bubbles and fewer small bubbles. Nucleation vs. growth can also be evaluated by finding the average bubble size by taking the ratio of the porosity and the bubble number density. Melt viscosity (controlled by composition, temperature, vesicularity, and volatile content, melt surface tension) and decompression

rate (controlled by ascent and complicated by stress fields and density) all affect whether a vesicular melt will have numerous small bubbles or fewer, larger bubbles (Burgisser and Gardner, 2004).

After nucleation, growth of bubbles and deformation of the surrounding melt occurs either by diffusing volatiles to, and increasing the moles of gas within, the bubble or by mechanically growing bubbles during decompression as the vapor phase expands and presses outward on the viscous surrounding melt. By assuming hexagonal close packing of bubbles suspended in melt, bubble growth can be modeled such that the behavior of every bubble in the system can be identically represented by a sphere of gas with radius R and an encapsulating shell of melt with shell thickness S-R (Proussevitch et al., 1993a). In this model, volatiles must diffuse through the melt shell and across the bubble–melt interface for bubbles to grow, which can limit bubble growth rates. Additional growth-rate limiting factors include the viscous resistance to the mechanical bubble expansion and changes in the solubility based on pressure and temperature fluctuations. When bubbles grow and thin the melt shells between them sufficiently, coalescence can occur as these shells break and bubbles join, resulting in increased bubble sizes, the formation of large gas slugs or pipes, and fragmentation. The growth, interaction, and interconnection of bubbles can have dramatic effects on the efficiency and style of degassing.

Chapter 1.4
Degassing Paths

We refer to the process of volatiles in magma exsolving to form a separate gas phase as degassing. In high viscosity melts with bubbles, each bubble is more likely to remain coupled with the surrounding melt, promoting efficient chemical exchange, which is described as closed-system degassing. The total mass of volatiles in the bubble and melt-shell must be conserved, which places controls on the gas-phase composition. If instead the gas phase is allowed to escape either through bubbles decoupling from and rising out of the melt in low viscosity magmas or through interconnection of bubbles and formation of gas channels, the degassing behavior is described as open-system and chemical exchange is not efficient. Whether the gas is removed from the system or not, if the vapor phase is allowed to stay in contact and equilibrate with the melt for long enough to not be diffusion or viscosity limited, equilibrium degassing will occur. In quickly ascending magmas, the high degree of underpressure can drive volatile exsolution from the melt faster than the volatiles can be transported through the melt to the vapor–melt interface, resulting in fractionation of volatiles through nonequilibrium degassing (Gonnermann and Manga, 2005b).

Degassing trends are often visualized using CO_2–H_2O plots as seen in Figure 1.3. Whether these trends represent open- or closed-system and equilibrium or nonequilibrium degassing determines how the gas phase and dissolved volatiles will evolve as depressurization drives exsolution. Additionally, open- system degassing allows bubbles to relieve overpressure from gas expansion and efficiently reduce vesicularity, regulating

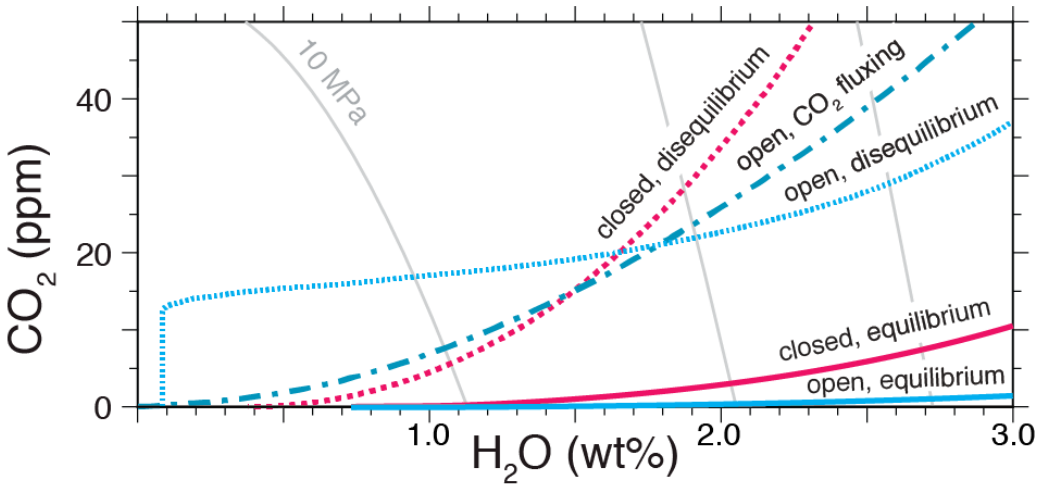

Figure 1.3. Different models showing late-stage, low-pressure degassing paths of H_2O and CO_2 concentrations in the far-field melt. Note equilibrium degassing's much lower CO_2/H_2O ratio compared to the nonequilibrium degassing paths. Open degassing paths are drawn in blue and closed in magenta. Solid gray lines show isobars at 800°C. Adapted from Watkins et al. (2017).

eruption style and governing whether volcanoes exhibit explosive or effusive behavior (Woods and Koyaguchi, 1994; Villemant and Boudon, 1998).

In equilibrium, open-system degassing, CO_2 will be efficiently and preferentially removed from the melt due to its lower solubility compared to H_2O. Once the majority of CO_2 is removed, if depressurization continues, H_2O will exsolve from the melt as well. This type of degassing will occur when interconnected bubble networks have very thin melt-shells such as in an auto-brecciating foam or in fragmented material above the glass transition temperature. Equilibrium, closed-system degassing will occur in slowly rising viscous magmas where the timescales of depressurization are greater than the timescales of CO_2 diffusion, the limiting diffusive species. Non-equilibrium degassing occurs when the timescales of depressurization are much lower than the timescales of diffusion, which primarily will occur during fast ascent with melt-shells with sufficient thickness for greater diffusive timescale of volatiles. Thus degassing style is primarily controlled by

ascent rate, the degassing history that came before (bubble size, spacing), and the diffusivities of volatile species.

Chapter 1.5
Observations of Non-Equilibrium Degassing

Recent studies of pyroclastic obsidians from the ca. 1340 A.D. Mono Craters have shown that these glasses can contain elevated CO_2/H_2O concentration ratios explained by nonequilibrium degassing during magma ascent (Gonnerman and Manga, 2005b). For nonequilibrium degassing to occur, suppressed nucleation is required to keep bubble number densities at or below 10^{11} m^{-3}, as the distance between bubbles has a strong control on equilibration time. Other studies have called upon the fluxing of a CO_2-rich vapor phase to buffer CO_2/H_2O concentration ratios, which is supported by recent findings of CO_2-rich, cuspate vesicles in some pyroclasts (Newman et al., 1988; Rust et al., 2004; Watkins et al., 2017). Preserved volatile concentration gradients in these pyroclasts have been used as geobarometers and evidence for temperature- and pressure-cycling of magma in the feeder system (Watkins et al., 2012; Watkins et al., 2017).

Chapter 1.6
Research Questions

Motivated by these recent observations of preserved, non-equilibrium degassing in natural rhyolitic glass, we seek to better quantify the effects of different parameters— such as bubble size, spacing, temperature, vapor composition, and ascent rate— on the vapor–melt re-equilibration time. To answer the questions of what the timescales of re-equilibration are after a perturbation in temperature or pressure and over what range of ascent rates is the assumption of vapor–melt equilibrium valid, we combine isothermal,

continuous-decompression experiments with numerical diffusion modeling in order to begin to constrain the characteristic timescale of diffusive equilibration (τ_{diff}). Better understanding of τ_{diff} will improve conduit models and allow for more accurate testing of the responses of conduits to different impulses occurring on the timescales of bubble growth and resorption such as sudden depressurization, rock falls in the conduits, and volcano–seismic interaction (Karlstrom and Dunham, 2016).

CHAPTER II

METHODS

Chapter 2.1
Capsule Assembly

The experimental design used in this study aims to replicate the closed degassing behavior of a parcel of magma that is first saturated with H_2O and CO_2 at shallow magma storage pressures and temperature and then ascends/depressurizes at a fixed rate to force dissolved volatiles to exsolve into or form bubbles. These experiments are adapted from the step-decompression experimental design of Yoshimura and Nakamura (2010a). The sample can be quenched to glass at any time during the experiment, allowing for analysis of saturated glass pre- and post-depressurization. In order to create the closed system, capsules were constructed from gold for its inert properties and welded shut in order to keep volatiles in contact with the melt and isolate the system from the pressurization medium, water.

The gold-tubing had an outer diameter of 3.5 mm and inner diameter of 2.5 mm (0.5 mm wall thickness). This tubing was first sectioned into ~22 mm segments using an X-Acto blade, and then was tri-crimped, trimmed, and welded shut on one end. Welding was performed under an argon atmosphere using a Lampert Puk-2 micro arc welder until shiny, overlapping welds capped the entirety of the crimped area. After being sealed at one end, the capsules were annealed in a furnace at 1000°C and atmospheric pressure for >3 hours to heal microfractures in the gold and reduce the likelihood of a leak exposing

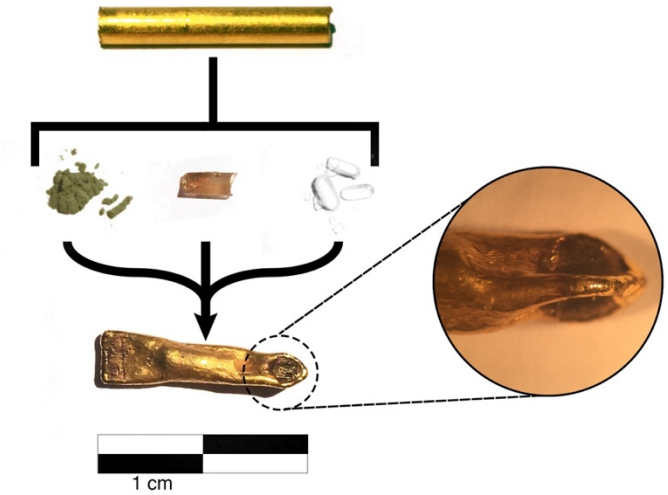

Figure 2.1. Photographs of capsule assembly components. From top to bottom: cut gold tubing; NNO, synthetic obsidian slab, and OAD crystals; completed and sealed experimental capsule post high temperature and pressure. Inset photo shows weld details.

Oxides	Mono-Inyo Craters (Newman et al., 1988)
SiO_2	76.45
Al_2O_3	12.32
CaO	0.52
MgO	0.01
FeO	1.02
TiO_2	0.059
Na_2O	3.80
K_2O	4.75
MnO	0.06
Total	98.99

Table 2.1. Bulk composition of rhyolitic obsidian used in experiments

the sample to the H_2O pressure medium. Images of the cut tubing, capsule components, and final construction can be seen in Figure 2.1.

Two different sample materials were used: natural obsidian from Panum Crater, Mono-Inyo Craters, California) and laboratory-synthesized obsidian of the same bulk composition (Table 2.1). Reagent-grade oxide powders were mixed, calcined, and melted at 1550°C for 24 hours, then crushed, powdered, and melted again at 1550°C for 24 hours to form the synthetic obsidian. The long annealing times were required to allow bubbles to escape, yielding an anhydrous, homogeneous, vesicle-free glass that was free of microlites. Sample material of both types was sectioned into rectangular slabs using a Bico diamond saw to dimensions of ~ 2 × 2 × 5 mm and rounded into cylinders using silicon-carbide sandpaper. Obsidian samples had an average mass of 0.036 ± 0.002 grams.

For all experiments, capsules were loaded with obsidian, oxalic acid dehydrate (OAD; $(COOH)_2 \bullet 2H_2O$) and a nickel-nickel oxide buffer (NNO) as shown in Figure 2.2.

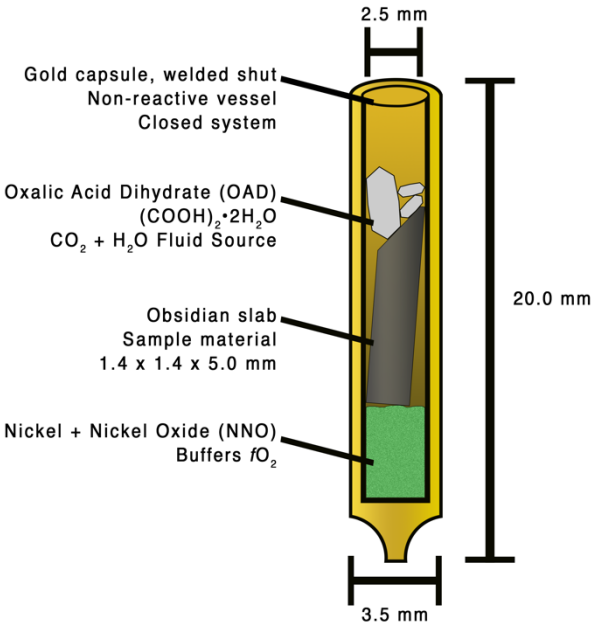

Figure 2.2. Schematic of a nearly-complete assembled capsule with all components Before loading into the pressure vessel, the top of the capsule will be flat-crimped and welded shut.

At high temperatures, the OAD decomposes to produce a H_2O–CO_2 fluid, the composition of which can be buffered to a binary mixture with the NNO powder (Matthews et al., 2003). Typically, about 0.04 grams of NNO (100% of the sample material by weight) was added and tamped down. The obsidian slab was then inserted with enough OAD added on top to create enough fluid to fully saturate the sample (15% of the sample material by weight, ~0.006 g). The capsules were then flat-crimped and welded, closing the system and completing capsule construction. Empty capsules were massed before loading and subsequently re-massed after every step in the loading process to record the masses of each capsule component. An example of the notes taken during the loading process can be seen in Table 2.2.

Table 2.2. Masses of capsule after addition of each component (+NNO, +OBS, +OAD) and masses of individual components of the capsule along with final weight to verify that the system remained closed through experimentation.

Chapter 2.2
The Rapid Quench Cold-Seal Pressure Vessel

After being loaded, sealed, and massed a final time, capsules were secured with nichrome wire in a sample holder and inserted into the bomb of the cold-seal pressure vessel (CSPV). The pressure was then increased to experimental conditions, and the furnace was lowered to bring the sample up to temperature. The CSPV at the University of Oregon, designed by Johnston and Senkovich (2007), allows for pressure and temperature conditions to be held constant for days, weeks, or whatever experiment duration is required. Thermocouples in the furnace and attached directly to the sample-holding bomb (made of René 41, a nickel based alloy) measured and maintained constant temperatures for the duration of the experiments. All experiments were run at 800°C. This temperature was chosen because it falls between the 790°C minimum temperature for Mono-Inyo Craters magma as determined by Fe-Ti thermometry and the 850°C maximum temperature for vesicle poor, volatile-rich glass before pumice formation occurs (Carmichael, 1967; Westrich, 1982).

	grams
Capsule	1.09727
+NNO	1.15604
NNO	0.05877
+OBS	1.19135
OBS	0.03531
+OAD	1.19741
OAD	0.00606
Final Weight	1.15968

The pressure can then be adjusted with a piston driven by a stepper motor, allowing for precisely held pressure levels as well as programmed decompression paths. After the goal of the experiment has been achieved (equilibration or decompression), a magnet is used to lower the sample holder from the heated bomb to a water-cooled jacket that quenches the sample to below the glass-transition temperature in a matter of seconds.

Once removed from the CSPV, capsules were weighed again to verify that the capsule remained a closed system and isolated from the pressure medium.

Chapter 2.3
Sample Preparation for FTIR Analysis

Samples were prepared for Fourier transform infrared (FTIR) analysis by the guidelines outlined in von Aulock et al. (2014). After weighing, capsules were affixed to a glass slide using Crystalbond 509 and bisected laterally with a diamond saw. One half of the sectioned capsule was set aside with the other half being was mounted in a puck of EpoKwick™ resin that was then allowed to cure overnight. Once hardened, the first face of the sample was polished using silicon carbide sandpaper of decreasing grit size in the sequence 800 → 1200 → 1500 → 2000 → 2500 → 3000. The face was then finished using 3 μm diamond grit until the surface reflected light with minimal visible scratches and flaws. To create a doubly polished wafer, we mounted singly polished pucks polished side down to a glass slide using Crystalbond 509 checking that no bubbles or excess Crystalbond were trapped under the sample to ensure the two polished faces would be parallel planes. The pucks were then laterally sliced on the diamond saw to create a ~1000 μm thick wafer. The polishing process was then repeated on the second side with a digital micrometer being used to ensure even thickness. Final thicknesses ranged from 100-400 μm and generally show cross sample thickness variation of <10%. After being fully polished to the final thickness, the Crystalbond 509 was dissolved using acetone, and samples were removed from the glass slide and set aside for FTIR analysis.

CHAPTER III

QUANTITATIVE ANALYSIS OF VOLATILES IN SILICATE GLASS USING FOURIER TRANSFORM INFRARED SPECTROSCOPY

3.1 Introduction

For over five decades now, Fourier transform infrared spectroscopy (FTIR) has been one of the most widely utilized analytical techniques for identifying and quantifying organic, polymeric, and inorganic substances with applications in fields ranging from materials science to forensics. Caltech's Edward Stolper developed the first volcanological application of the method in 1982 as introduced in his paper *Water in Silicate Glasses: An infrared spectroscopic study*. In the decades since, the technique has seen much refinement and has become a standard instrument in the volcanologist's toolbox.

This primer will focus on the application of FTIR analysis to quantify the dissolved volatile content in silicate glasses with a specific focus on H_2O and CO_2, the two most important volatiles in determining magma properties and eruptive behavior (e.g. Zhang 1997b; Shaw, 1972). This study used the transmission spectra method on rhyolitic samples, so the scope of this guide is limited to that technique. If further discussion on other FTIR techniques such as reflected light and attenuated total

reflectance (ATR), please refer to Brian Smith's book *Fundamentals of Fourier Transform Infrared Spectroscopy* (v.1,1995).

3.2 The Advantages of FTIR

The proliferation of FTIR as an analytical technique can mainly be attributed to instrument and maintenance cost, availability, and ease of use. This is not to say that spectroscopy is a wholly inferior technique to similarly applied microanalytical instruments such as attenuated total reflectance spectroscopy (ATR) and secondary ion mass spectrometers (SIMS), but each of these methods come with their own strengths and weaknesses (see Table 3.1). The main limitations of transmission FTIR appear when trying to make maps of resolution less than 25 μm or when analyzing samples with abundant bubbles, microlites, and inclusions, which will all decrease the fidelity of the spectrum.

Table 3.1. Strengths and weaknesses of common micro-analytical techniques

	Pros	**Cons**
Transmission FTIR (this study)	• High sensitivity for H_2O and CO_2 • Analysis is non-destructive to sample	• Requires doubly-polished samples • Spatial resolution limited to 25-35 μm
Synchrotron FTIR	• Spatial resolution diffraction limited down to 3-5 μm	• Very few synchrotrons available • Beamtime is costly and must be scheduled
ATR-FTIR	• Single polished surface required • Surface-only analysis ignores non-surface bubbles and microlites	• Only surface is analyzed • H_2O analysis only (no CO_2) • Requires FTIR and ATR accessory
nanoSIMS	• Extremely high spatial resolution (down to 0.05 μm) • High sensitivity (ppm) • Singly-polished samples	• Very few nanoSIMS available • Leaves pits in sample • Sample must be coated in carbon, gold, or platinum

3.3 Spectroscopy

All materials at temperatures above absolute zero give off black-body radiation. This radiation spectrum is composed of photons with a broad band of wavelengths (Figure 3.1). The intensity of this radiation scales exponentially in intensity and inversely in average wavelength (λ) with temperature. Planck's theory tells us that the energy of an individual photon scales solely with the photon's frequency (or inversely with wavelength). When this radiation passes through a material such as a sample of hydrous obsidian, photons of specific energies— and therefore wavelengths— match the harmonic energies of certain bond vibrations including stretching and bending. When this happens, the photon is absorbed rather than passing through the sample and reaching a detector. Over a broadband spectrum of diverse wavelengths, all species of interest possessing absorbing bonds will appear as a drop in intensity at the associated wavelength for the specific bond (Figure 3.1B). The ratio between the original blackbody curve and the interfered curve can then be converted to a transmittance spectrum, which is then inverted to make an absorbance spectrum (Figure 3.1C). The amount of light that is absorbed scales with the thickness of the

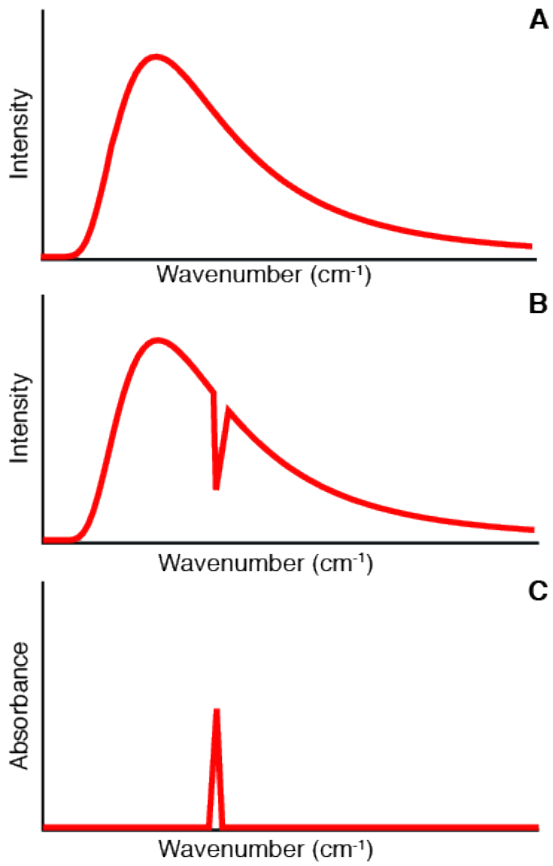

Figure 3.1. Schematic example of a broadband blackbody spectrum (A) with single negative interference peak reducing intensity at a specific wavelength representing one species (i.e. CO_2) (B) and converted to an absorbance spectrum with a positive peak at the same wavelength (C).

sample and concentration of the bond in question. This relationship, known as Beer's Law, is the foundation for quantitative spectroscopy.

With the absorbance of each species of interest and thickness of the sample known, the concentrations of each species can be calculated with precision and accuracy as follows:

$$c = \frac{MA}{\rho d \varepsilon} \tag{3.1}$$

where C is the concentration of the species of interest, M is the molecular weight of the species (g/mol), A is the measured absorbance peak, ρ is the density of the sample glass (g/L), d is the thickness of the sample (cm), and ε is the molar absorption coefficient (L/mol/cm).

For the analysis of H_2O in silicate glass samples with significant water content (> ~0.5 wt.%) and thickness of several hundred microns, the secondary harmonic bending in the near-IR region (6000-4000 cm^{-1}) are used, as the first harmonic oscillation blocks too much light for the peak to be resolved. Absorption peaks and spectral features are described by their wavenumber (cm^{-1}, the inverse of the wavelength) in order to make peaks easily differentiable with numbers of tangible scale. In this study, the water species of interest are molecular H_2O and structural OH, which have absorbance peaks at 5230 cm^{-1} and 4520 cm^{-1} respectively (Stolper, 1982). These peaks correspond to the OH stretching and HOH bending of H_2O and stretch of the OH molecule (see Figure 3.2). The comparatively low abundance of CO_2 in the samples (measured in ppm rather than

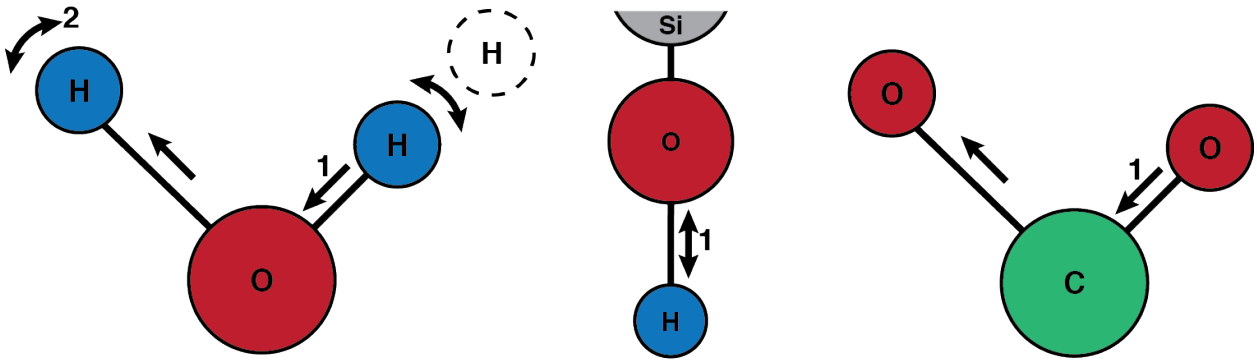

wt. %) allows for the primary peak within the mid-IR region at 2350 cm^{-1} from the asymmetric stretching mode (Figure 3.2) to be measured.

3.4 How the FTIR Works

Fourier transform infrared spectroscopy possesses numerous benefits that have led to the almost total displacement of dispersive spectroscopy when doing IR analysis. These advantages arise from the fact that rather than the dispersive spectrometer's limitation of examining intensities for only single wavenumbers at a time, all wavenumbers in the spectrum can be measured in the time it takes to do a single scan, occurring multiple times a second. This gives FTIR what is known as the multiplex

Figure 3.2. Illustration of the vibrational modes of molecular H_2O, OH, and CO_2. H_2O (m) has two vibrational modes, and the near-IR peak is located at 5230 cm^{-1}. OH and CO_2 each have one vibrational mode and can be measured by their absorption peaks at 4530 cm^{-1} and 2350 cm^{-1} respectively.

advantage that yields a higher signal-to-noise ratio (SNR) due to the fact that the noise is measured at all wavenumbers for the entire analysis. High SNRs lead to clear signals and better measurements. Longer measurement times reduce noise because if noise is truly random, it has a tendency to cancel itself out, as the sign of the noise has an equal probability of being positive or negative. The number of scans at an individual spot can

be increased in order to improve SNR, but as the SNR is proportional to the square root of the number of scans (i.e. SNR ~ [# scans]$^{1/2}$), there are diminishing returns that may not be offset by the increased measurement time and possibility of instrument "drift" error to occur. In order to get the best analysis possible, some choices must be made and balances must be struck when setting up the instrument and preparing your sample.

The path of the infrared beam in the FTIR can be split into four sections (Figure 3.3). In order of travel, these sections are the source, interferometer, sample, and detector. In the Nexus 670 ThermoNicolet FTIR Spectrometer at the University of Oregon, two sources are available: an ETC EverGlo mid-IR source (9600-20 cm^{-1}) and a Tungsten-

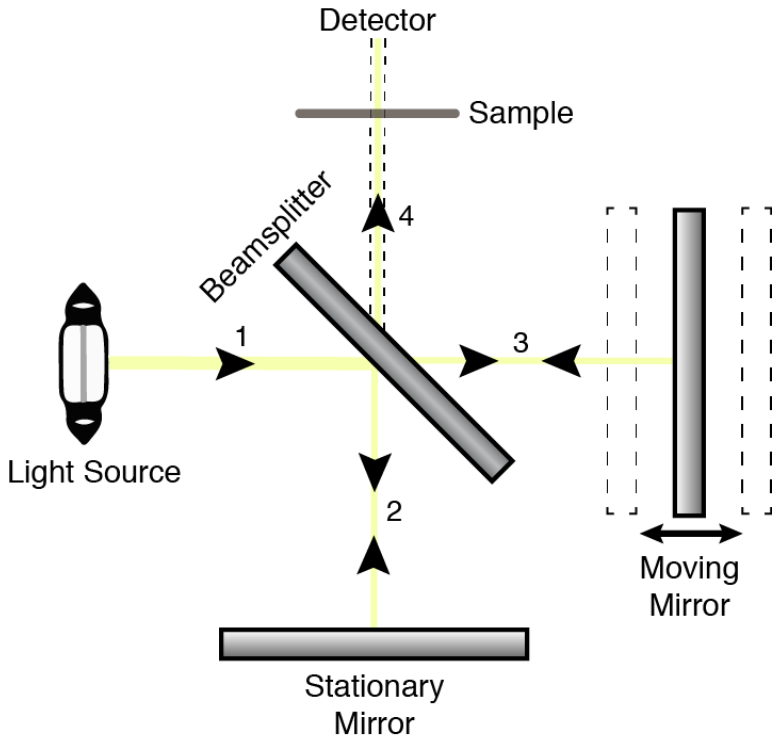

Figure 3.3. Light path through the FTIR spectrometer
1 Source emits coherent spectrum
2 Beam is split, half the light goes to stationary mirror to be reflected back
3 Other half of light hits moving mirror, which changes the distance of the light path
4 Light is recombined then travels through the sample and to the detector, difference in light path difference will determine amount of interference

Halogen white light source (27000-2000 cm^{-1}). The white light source provides a higher SNR in the near-IR region than the mid-IR source, which is desirable in this rhyolite study because of the near-IR peaks of the H_2O (m) and OH species of interest. The white light is more effective in the near-IR because although the peak is centered outside of the IR range, the intensity of white light is higher, which carries over to the adjacent near-IR range as well. In a basalt study, the white light source would not be appropriate, as the CO_3 doublet peak at 1430 cm^{-1} would be missed, so the desired species to be analyzed will determine which source is used.

From the source, the light travels into the Michelson interferometer. The combined pair of the interferometer and the Fourier transform are the key to FTIR analysis, allowing the spectrum to be analyzed as a whole rather than piecemeal. First, the light travels through a K-Br beamsplitter that sends an equal amount of light to a stationary mirror and a moving mirror. As the moving mirror changes the length of the path that one light beam travels, the difference in the path distance between the light that goes to the stationary mirror and the moving mirror will cause constructive or destructive interference in the recombined beam that depends on how out of phase the two beams are. When the path lengths are equal (or different by $n \times \lambda$ where n is an integer), the beams are said to be in phase and have purely constructive interference. When the path difference is zero (known as the zero path difference, ZPD), the detector will see the maximum amount of light.

When the beams are fully out of phase (different by $n\times\lambda+\lambda/2$), they have purely destructive interference, and the detector sees the minimum amount of light, which should theoretically be zero. At path differences between fully in and out of phase, the beams experience a combination of constructive and destructive interference. As the moving mirror sweeps through a range of distances, each of an array of wavelengths experiences destructive interference at a wavelength dependent distance away from the ZPD, and the detector registers a range of intensities. The plot of these intensities versus the path difference is known as an interferogram. As the light source is broadband and contains a wide range of wavelengths, each with their own intensity, the interferogram represents a complex summation of many wavelengths interfering constructively and destructively at once. The exception to this is at the zero path difference where all wavelengths interfere constructively. The interferogram can then be said to be "encoding" the intensities of every wavelength in a single scan. An example of this can be seen in Figure 3.4. As the detector can only register intensity as a one-dimensional voltage value, this allows the whole spectrum to be analyzed in a single sweep of the path difference, which can be done much more quickly than cycling through the entire spectrum with a monochromatic source.

The FTIR spectrometer at the University of Oregon uses a mercury-cadmium-telluride (MCT-A) detector, which is highly sensitive to very small amounts of IR radiation over a range of wavenumbers from 600-11,700 cm^{-1}. This detector has a maximum intensity it can measure however, which prevents the usage of the main water peak (3550 cm^{-1}) for analysis of hydrous rhyolite samples at the thicknesses our samples

are prepared at. Fortunately, the near-IR provides highly resolvable peaks that give important information about water speciation.

To deconvolve these complex interferograms back into spectra, a Fourier transformation is required. A Fourier transform takes a function and breaks it down into a summed series of sine functions each with their own amplitude and periodicity, a process that can be performed for any continuous function. These amplitudes and periodicities correspond to the intensities of light at specific wavenumbers, which can then be plotted as a spectrum. Due to the number of sine functions required to make a complete spectrum, this is a computationally intense process that was not feasible before the advent of computers and development of the fast Fourier transform (FFT) algorithm. This method, commonly known as the Cooley-Tukey algorithm, was developed in 1965,

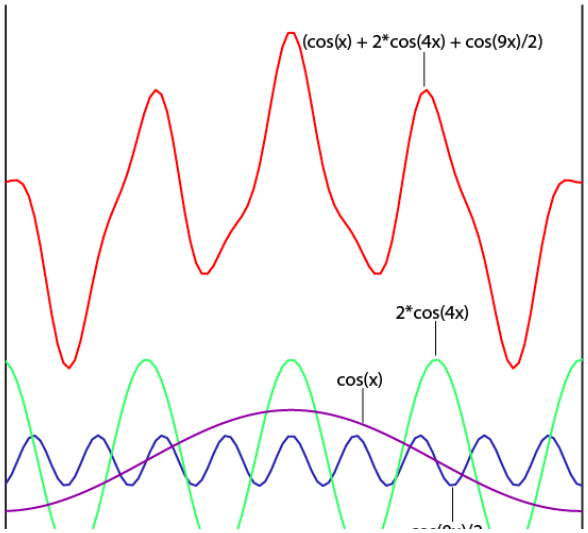

Figure 3.4. A simplified interferogram (red) is constructed from waves of different wavelength and amplitude (purple, green, and blue). During FTIR analysis, every wavelength in the range of light being looked at contributes an intensity resulting in the complicated interferograms seen during benchmarking.

which directly resulted in the proliferation of FTIR analysis in the years after (Cooley and Tukey, 1965; Forman, 1966).

There are two types of spectra needed to perform FTIR analysis: sample spectra and background spectra. The background spectra are simply spectra where the light does not pass through the sample when it travels from the interferometer to the detector. By dividing the sample spectrum by the background spectrum and inverting the result, an absorbance spectrum is created from which the absorbance of species of interest can be measured. When measuring these absorbance values, the height of the peak is measured. These peaks often occur on a larger slope, so a baseline is taken by drawing a line from the left extent of the peak to the right extent and measuring the peak height value from that baseline. Once the baseline is determined, the absorbance values for a peak (e.g. the 2350 cm^{-1} CO_2 peak) for all measured points will be outputted for use in quantitative analysis.

Sample material and preparation controls many of the decisions one makes when performing FTIR analysis and must always be considered. The largest source of error can usually be attributed to poor sample preparation. In this rhyolitic glass study, samples must be checked for inclusions such as microlites and bubbles that may obstruct and scatter beam. Additionally, the level of translucency of the sample will determine how thin sample wafers need to be, as light needs to be able to pass easily through the sample. Samples must be polished to a minimum of 1 μm on both sides to a thickness of 100-500 μm depending on sample translucency. Care must be taken to ensure that both sides are

planar and thickness is uniform across the sample. Failure to ensure uniform thickness can lead to error across the sample when concentrations are calculated.

For this study, 64 scans were performed for each spot at a spectral resolution of 8 cm^{-1}. These values were chosen to balance measurement time and SNR quality. As mentioned before, SNR increases with the square root of the number of scans, so a doubling in the number of scans doubles measurement time but will only increase SNR by a factor of ~1.4. Measurement time needs to be minimized not only for the sake of expediency, as if measurements take too long, the instrument can experience drift and maybe give subtly different values at the same spot between a measurement made at the beginning of a long run and a measurement made at the end. Additionally, the detector requires liquid nitrogen to be cooled, which lasts about 6 hours before needing to be refilled. The spectral resolution chosen will depend on the width of the peaks being examined. An increase in the spectral resolution also increases the SNR, but may reduce the fidelity of the measurement of thin peaks. In this study, a resolution of 8 cm^{-1} is more than adequate to capture all the detail required.

3.5 Quantitative Analysis

In this study, we calculate the concentrations of three volatile species using Beer's Law (see equation 1): molecular water (H_2O_m), structural water (OH), and carbon dioxide (CO_2). A constant density of 2277 g/L for the glass is assumed, the Newman et al. (1988) value for Mono-Inyo obsidian. Thickness is measured at multiple points and averaged for the sample using digital micrometers with an accuracy of ±2-3 μm. For all samples, the CO_2 molar absorption coefficient remains constant, but the molar absorption of H_2O

depends on H_2O concentration. These coefficients are empirically quantified by dissolving pure H_2O or CO_2 in an artificial magma at high temperatures and pressures and quenching it quickly to glass (Zhang et al., 1997b, Behrens et al., 2004). The spectrum is then measured and absorbance values calculated. To find the volatile concentration to back calculate the molar absorption coefficients, the sample is then heated in a vacuum to remove all volatiles and weighed to calculate the weight percentage of the specific volatile species (Newman et al., 1986). Knowing thickness and density of the sample, concentration, and absorbance, ε can then be calculated. Molar absorptivities are highly dependent on silica content and must be recalculated for highly varying magmas.

CO_2 content can be simply calculated using Beer's Law with an ε=1214 L/mol/cm, as only one CO_2 species is present (Behrens, 2004). In more mafic samples with CO_2 complexes, this assumption would not be valid (Fine and Stolper, 1985; Duncan and Dasgupta, 2015). As H_2O speciates into H_2O_m and OH in rhyolites at these temperatures, the ε values for each species depends on their relative abundances. This relationship was originally quantified by Newman, Stolper, and Epstein and improved by Zhang et al. in 1997b. This modified Beer's Law equation appears as follows:

$$\frac{\rho}{\rho_0} C_{H_2O_m} = a_0 \bar{A}_{5230} \tag{3.2a}$$

$$\frac{\rho}{\rho_0} C_{OH} = (b_0 + b_1 \bar{A}_{5230} + b_2 \bar{A}_{4520}) \bar{A}_{4520} \tag{3.2b}$$

$$C_{H_2O_t} = C_{H_2O_m} + C_{OH} \tag{3.2c}$$

$$a_0 = 0.04217 \text{ mm}$$

$$b_0 = 0.04024 \text{ mm}$$

$$b_1 = -0.02011 \text{ mm}^2$$

$$b_2 = 0.0522 \text{ mm}^2$$

Where $\bar{A}$ is the absorbance divided by the thickness in mm and $\frac{\rho}{\rho_0}$ equals the ratio of the density of hydrous to anhydrous melt, which are assumed to be equal in this study. Using this equation, the concentrations of the individual hydrous species can be found and summed to find the total H_2O weight percentage (wt.%) of the sample. Temperature controls the initial speciation of the hydrous species before cooling, but speciation during cooling records quench rates and provides a useful geospeedometer (Ihinger et al., 1997; Zhang et al. 2000).

Knowing the location of where each sample is taken, concentration data can be mapped spatially to one-dimensional transects or two-dimensional areas, generating concentration profiles or heat maps of volatile contents. This measured spatial data can then be used to constrain models of volatile diffusion, bubble growth/resorption, ash sintering, and other micro-scale conduit processes.

CHAPTER IV

STEP-DECOMPRESSION MODELING METHODS, RESULTS, AND DISCUSSION

4.1 Step-Decompression Model Methods

An understanding of the timescales of bubble growth and equilibration is vital for the modeling of conduit processes. To this end, we adapted a one-dimension numerical MATLAB model from Aster et al. (2016) to test sensitivity of equilibration time for a fully saturated, instantaneously decompressed system to variable bubble-size, bubble-spacing, pressure-drop magnitude, temperature, and initial CO_2/H_2O ratio.

We define the characteristic timescale of equilibration (τ_{diff}) to be the time from onset of depressurization for the difference in initial CO_2 concentrations between the far-field melt and vapor–melt interface to reduce by a factor of *e* (Figure 4.1, Figure 4.2). To find this timescale, our model takes the temperature of the melt in °C, starting pressure in MPa, ending pressure, initial H_2O concentration in wt. %, bubble spacing in microns, and bubble radius in microns as initial parameters.

Initial CO_2 concentrations in the saturated melt are determined using the pressure, temperature, and vapor composition H_2O–CO_2 solubility relationship described in Liu et al. (2005). Then, the pressure can be dropped instantaneously or continuously with CO_2 and H_2O concentrations being recalculated at the first and last nodes using known solubility

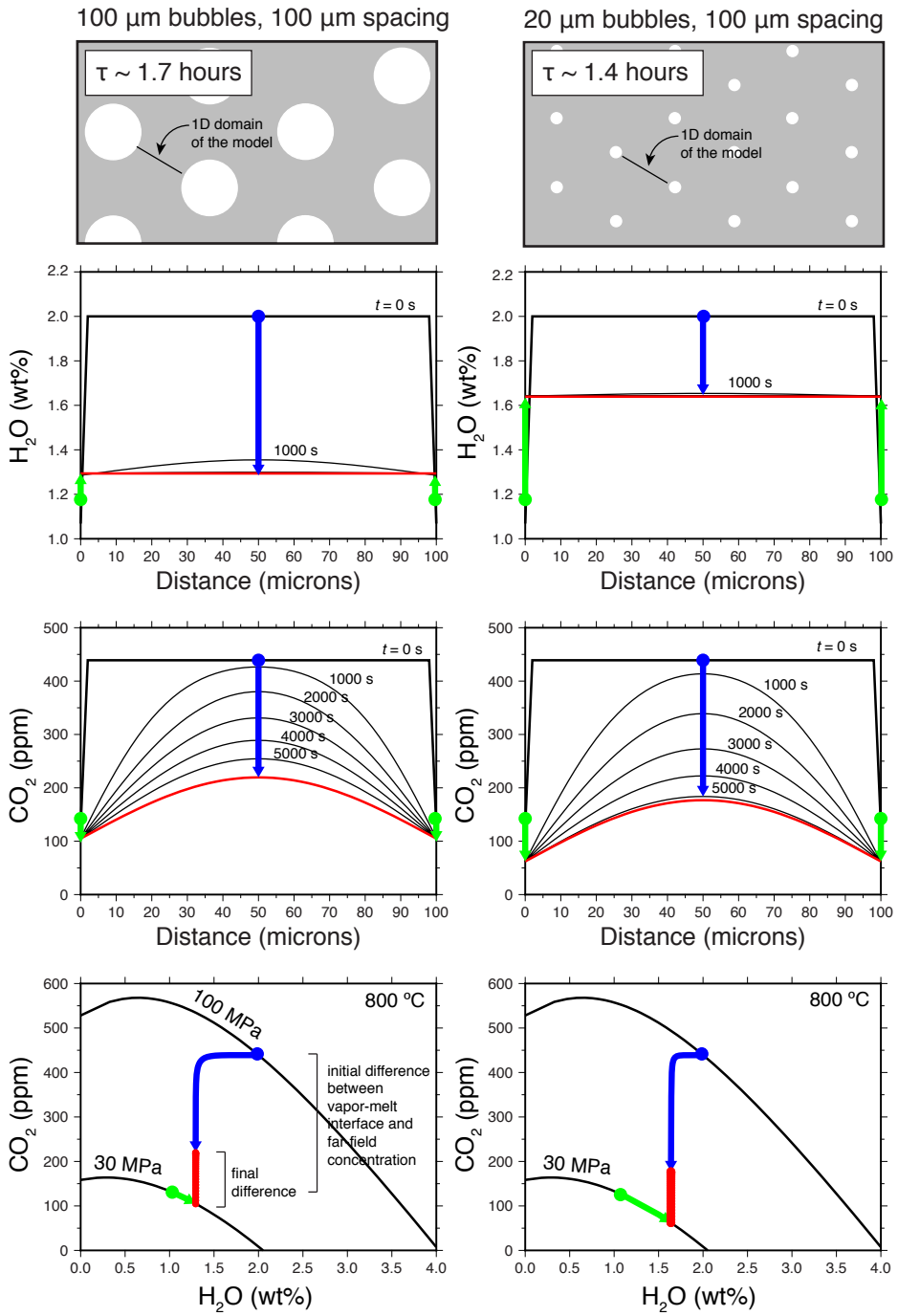

Figure 4.1. Schematic illustration of two different model runs. Both models calculate the equilibration time, τ_{diff}, for an instantaneous pressure drop from 100 to 30 MPa at 800°C. The left column shows the results from a run with 100 µm bubbles spaced 100 µm apart, and the right column shows the same results from a run with 20 µm bubbles spaced 100 µm apart. The next two rows of panels illustrate how H_2O and CO_2 concentration profiles evolve until the CO_2 concentration hits the predetermined *e*-folding equilibration conditions (profile drawn in red). The bottom row displays the evolution of the dissolved volatile concentrations in the far-field melt (blue) and at the vapor-melt interface (green) along with the final concentration profile (red).

relationships. The mole-flux boundary condition at the vapor–melt interface tracks the moles of vapor in the bubble and the flux of volatiles across the vapor–melt interface, conserving mass. The vapor–melt boundary is then updated first with the assumption of local equilibrium between the exsolved volatiles and immediately adjacent melt.

With a concentration gradient present between the vapor-melt interface and the now supersaturated melt, diffusion of volatiles through the melt can occur. The change in concentration of dissolved volatile species is calculated using the one-dimensional diffusion equation in spherical coordinates:

$$\frac{dC}{dt} = \frac{1}{r^2}\frac{d}{dr}(Dr^2\frac{dC}{dr}) \tag{4.1a}$$

With *C* being dissolved volatile concentration in melt at distance *r* from the center of the bubble and *D* being the diffusivity of the same volatile species at point r. For numerical purposes, this equation can then be discretized as

$$C_r^{t+1} = \left(\frac{dD}{dr}\frac{dC}{dr} + \frac{2}{r}D\frac{dC}{dr} + D\frac{d^2C}{dr^2}\right)dt + C_r^t \tag{4.2a}$$

where

$$\frac{dD}{dr} = \frac{D_{r+1} - D_{r-1}}{2dr} \tag{4.2b}$$

$$\frac{dC}{dr} = \frac{C_{r+1}^t - C_{r-1}^t}{2dr} \tag{4.2c}$$

$$\frac{d2C}{dr^2} = \frac{C_{r+1}^t - 2C_r^t + C_{r-1}^t}{dr^2} \tag{4.2d}$$

The diffusivities of H_2O and CO_2 in rhyolite melt depend on water content and temperature as follows (Zhang and Ni, 2010):

$$\ln(D_{H_2O}) = -14.26 + 1.888P - 37.26X - \frac{12939 + 3626P - 75884X}{T} \quad (4.2)$$

$$\ln(D_{CO_2}) = -13.99 - \frac{17367 + 1944.8P}{T} + \frac{8.552 + 271.2P}{T} C_w \quad (4.3)$$

Where D is in m^2/s, T is in K, P is in GPa, X is mole fraction of H_2O, and C_w is wt. % of H_2O. The diffusivity of both volatile species is highly dependent on H_2O concentration and can significantly vary spatially depending on local H_2O concentration.

In addition to assuming local equilibrium at the vapor-melt interface, the model assumes that bubbles are spherical, evenly spaced and sized, and are coupled to the melt; no other volatiles affect the solubility or diffusion of H_2O and CO_2; and that volatile transportation is a purely diffusive process and no advection takes place. We define τ_{diff} to be the *e*-folding time of the difference between far-field and vapor–melt CO_2

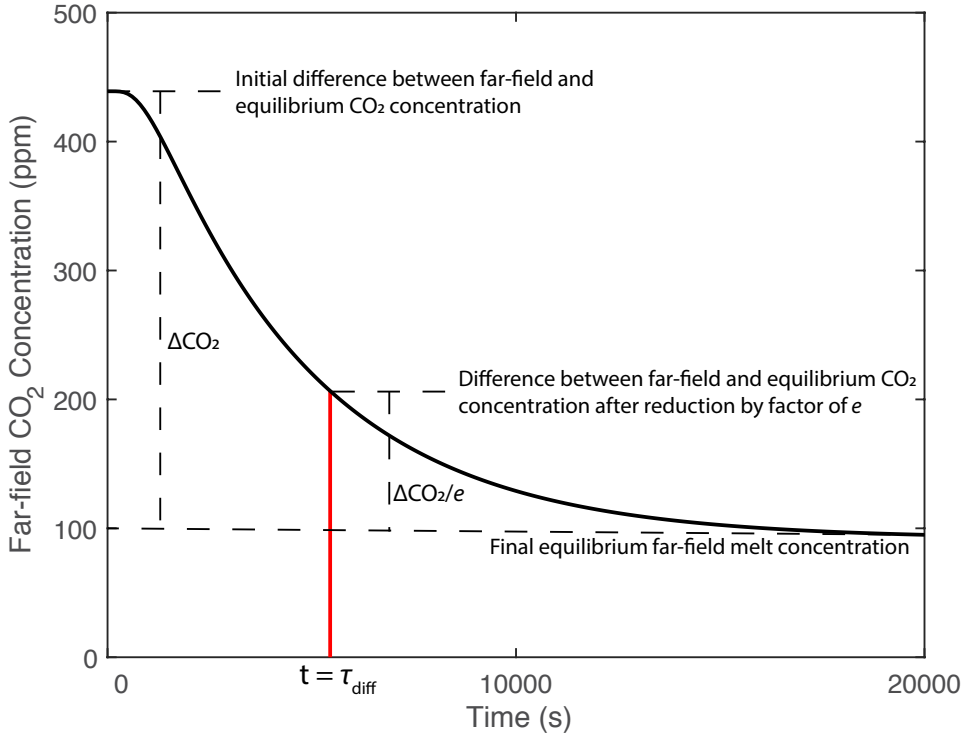

Figure 4.2. Evolution of the far-field melt CO_2 concentration after instantaneous decompression from 100 to 30 MPa at 2 wt.% initial water content, 800°C for far-field melt between 100 µm diameter bubbles with 100 µm spacing.

concentrations, as the evolution of far-field melt concentration can be approximated by exponential decay as seen in Figure 4.2.

4.2 Step-Decompression Modeling Results

In order to test the sensitivity of equilibration time to various parameters, we fix all variables except the variable of interest, which is varied across a range of realistic values. For bubble radii ranging from 1-1000 microns and spacing ranging from 50-500 microns, we produced a range of values for τ_{diff} that cover two orders of magnitude (Figure 4.3). Readily apparent is the significant factor of bubble-spacing on τ_{diff}, which exponentially increases the time required for bubble–melt equilibration. Bubble-size also positively affects equilibration timescale but has a subordinate effect to bubble-spacing.

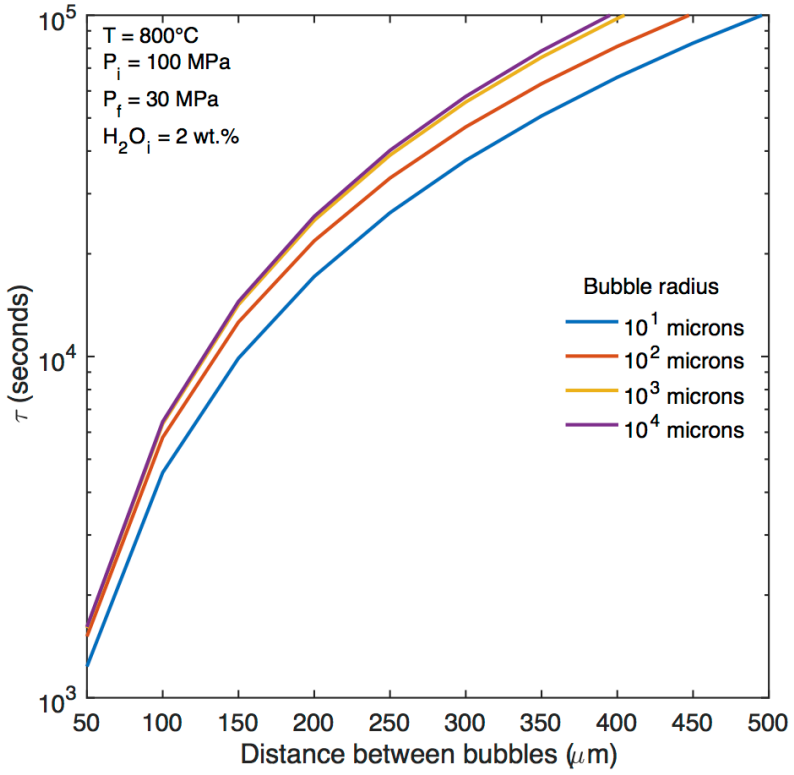

Figure 4.3. Results of calculating equilibration timescales of bubbles varying 1-1000 µm in radius and with spacing ranging from 50-500 µm apart after a pressure drop of 100 to 30 MPa at 800°C with 2 wt. % starting H_2O.

In addition to bubble-size and bubble-spacing, we systematically varied temperature, pressure-drop magnitude (by varying final pressure), and initial CO_2/H_2O ratio to quantify how these different variables affect equilibration time (Figure 4.3-4.7). As predicted by diffusivity relationships (Zhang and Ni, 2010), temperature has strong control on equilibration time with a 100°C temperature increase resulting in an order of magnitude decrease in equilibration time (Figure 4.4). Bubble-spacing and temperature have the greatest effects on equilibration time with pressure-drop magnitude and CO_2/H_2O ratio having lesser effects. Modeling the response to pressure-drop magnitude (ΔP)—in this case varied by changing the final pressure (i.e. starting pressure was held constant at 100 MPa for all runs)—resulted in a near-flat profile of the response of equilibration time to ΔP until large pressure changes (>80MPa) were experienced (Figure 4.5). A 100 MPa pressure change (decompressing from 100 MPa to 0 MPa) resulted in an equilibration time 4 times longer than those modeled for small pressure drops. Varying the initial pressure from 50 to 100 MPa with a constant 50 MPa pressure drop results in a

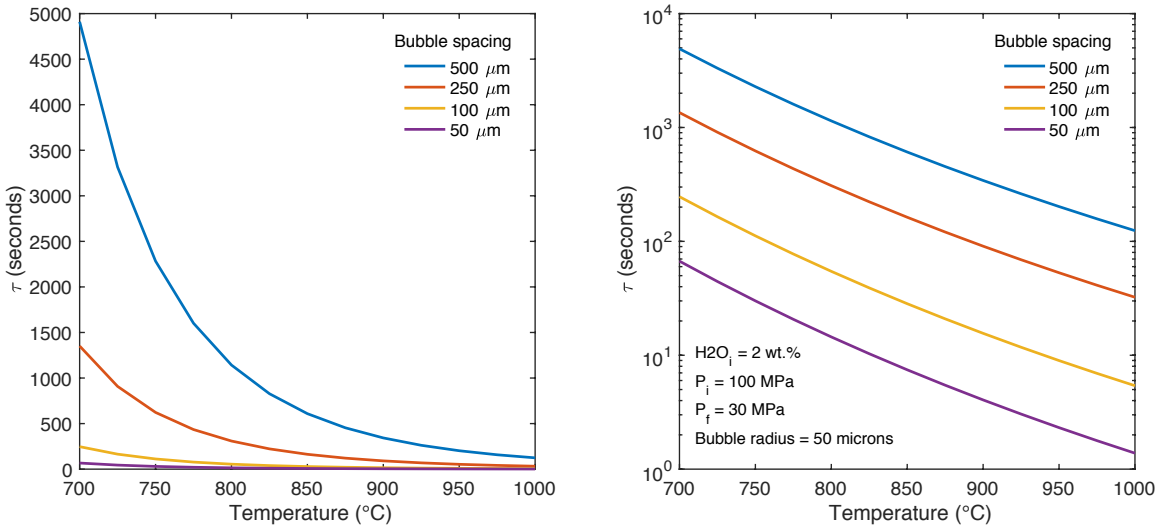

Figure 4.4. Equilibration time plotted against temperature of model run for a variety of temperatures ranging from 700-1000°C and bubble spacing ranging from 50-500 μm. Both plots show the same data with the right hand side plotting equilibration time in log space to show that temperature doesn't change the sensitivity of equilibration time to bubble-spacing and vice-versa.

roughly fourfold decrease in in equilibration time, but increasing the pressure past that has no effect. When the initial CO_2/H_2O ratio is varied, and thus starting H_2O content, the addition of a small amount of water (<0.2 mole fraction) results in a rapid fall in

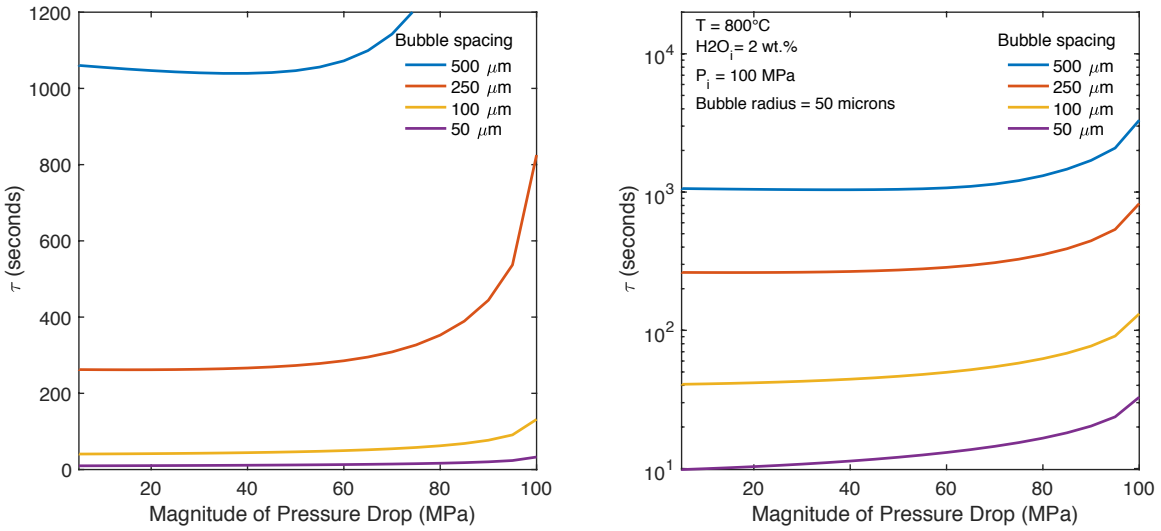

Figure 4.5. Equilibration time plotted against pressure-drop magnitude of model run for a variety of ΔP ranging from 0-100 MPa with bubble spacing ranging from 50-500 μm. Both plots show the same data with the right hand side plotting equilibration time in log space to show that ΔP doesn't change the sensitivity of equilibration time to bubble- spacing and vice-versa.

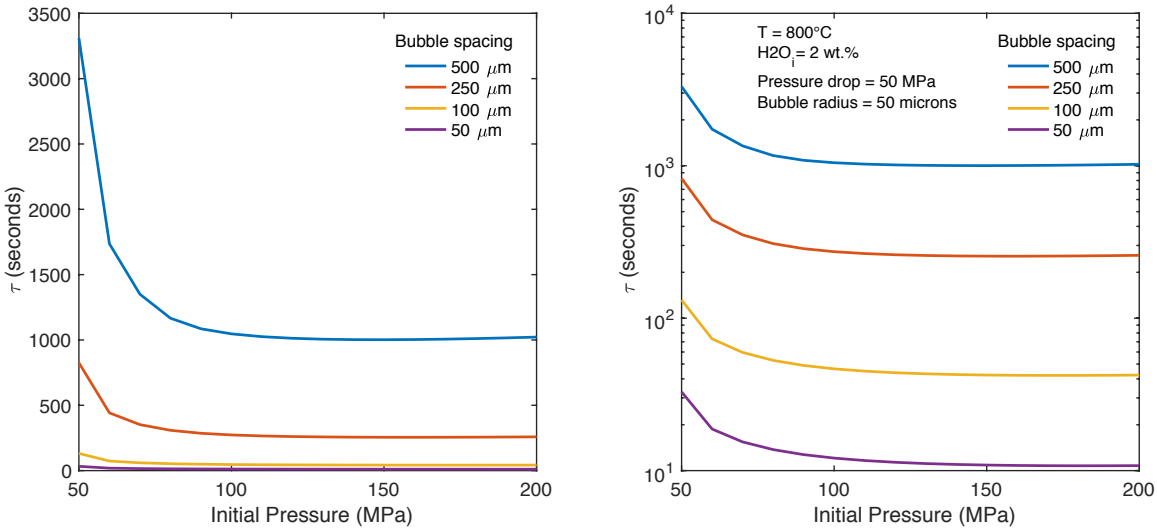

Figure 4.6. Equilibration time plotted against initial pressure of model run for a variety of P_i ranging from 50-200 MPa with a 50 MPa pressure drop and bubble spacing ranging from 50-500 μm. Both plots show the same data with the right hand side plotting equilibration time in log space to show that P_i doesn't change the sensitivity of equilibration time to bubble- spacing and vice-versa.

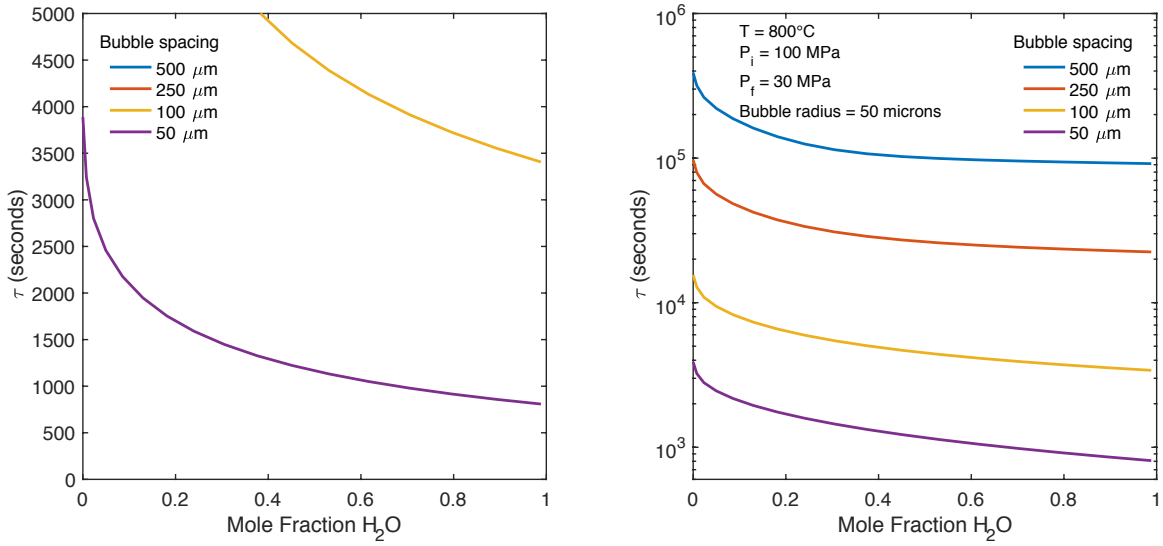

Figure 4.7. Equilibration time plotted against mole-fraction H_2O of model run for a variety of X_{H2O} ranging from 0-1 with bubble spacing ranging from 50-500 μm. Both plots show the same data with the right hand side plotting equilibration time in log space to show that X_{H2O} doesn't change the sensitivity of equilibration time to bubble-spacing and vice-versa.

equilibration time by a factor of 4 (Figure 4.7). After the initial addition however, the effect of adding additional water on equilibration time falls of significantly.

4.3 Continuous-Decompression Modeling Results

After testing the sensitivity of equilibration time to different variables, we modified the numerical model for checking whether equilibrium is sustained during continuous decompression (Figure 4.8). The model runs are set up in the same way, except now the parameters being varied are decompression rate and bubble spacing, and we define a run to be a case of equilibrium degassing if, at the time the final pressure is reached, the difference between far-field melt and vapor–melt interface has reduced from its initial condition by at least a factor of *e*. When plotted in log-log space, the regions of equilibrium and non-equilibrium degassing are able to be clearly demarcated by a straight line. In all cases, increasing decompression rate drives the system towards non-

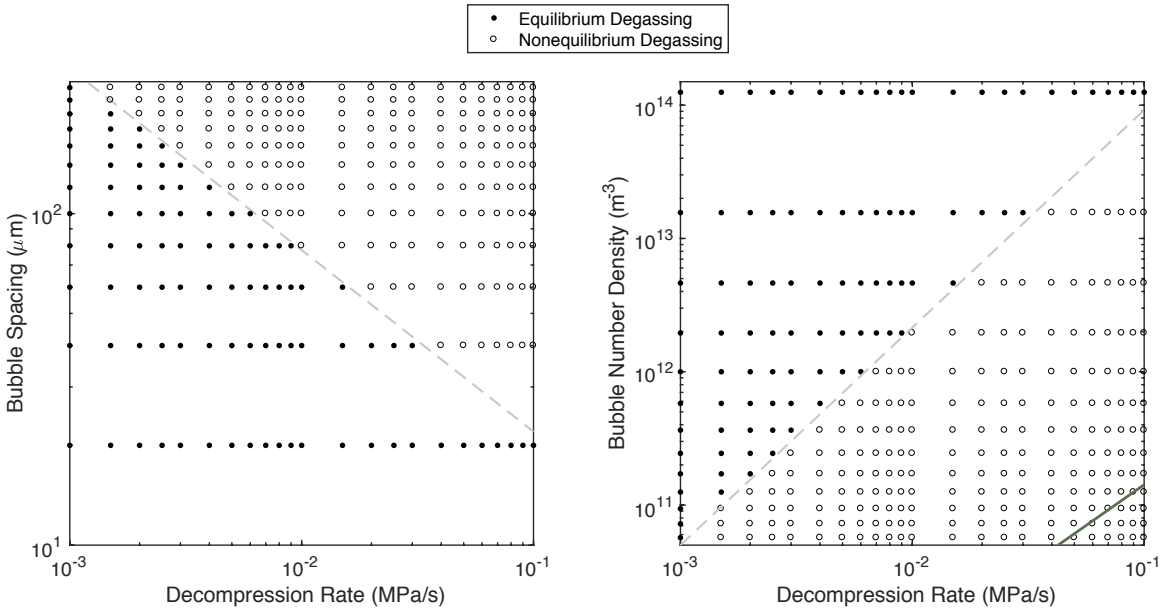

Figure 4.8. Results of continuous decompression model runs with variable decompression rate and bubble-spacing/BND. Model runs representing equilibrium degassing marked with filled point and nonequilibrium degassing marked with open point. All runs represent decompression from 100 to 30 MPa with constant temperature of 800°C, 2 wt.% initial water content, 100 μm bubble spacing, and 100 μm bubble diameter. Left plot shows bubble-spacing vs. decompression rate with the right plot displaying the same data with bubble-spacing converted to bubble number density, assuming evenly distributed bubbles in a melt. Solid line in right plot shows experimentally predicted BND vs. dP/dt for rhyolite at 800°C with heterogeneous nucleation occurring (Fiege and Cichy, 2015).

equilibrium degassing, and increasing bubble number density (decreasing spacing) drives the system towards equilibrium degassing.

4.4 Discussion

The two main ways variables affect equilibration time are by changing the distance that material must diffuse across and by affecting the rate (diffusivity) that volatiles can travel. Bubble size affects timescales by controlling the final vapor composition of the bubble-melt system, which considerably affects diffusion rates by changing water content in the melt. Large bubbles require more moles of water to reach

equilibration, which lowers the overall water concentration in the melt compared to small bubbles and slows diffusion rates. Bubble spacing increases both the quantity of volatiles to transport and distance that dissolved volatiles must diffuse, which results in the roughly squared dependence of τ_{diff} on bubble spacing, as predicted by the general diffusion scaling relationship:

$$\tau \sim \frac{L^2}{D} \tag{4.4}$$

where τ is the characteristic timescale of diffusion, D is the diffusivity, and L is the characteristic length scale. Temperature directly affects equilibration time by either speeding diffusion at higher temperatures or slowing diffusion at lower temperatures. Similarly, starting water content affects diffusion rates, although this effect diminishes after the addition of a small amount of water, which depolymerizes the melt, as seen in Figure 4.7.

This model does not allow for deformation and thinning of the melt-shell as the bubble grows, so it is only valid for cases of minimally growing bubbles with constant melt-shell thicknesses. For these cases, we tested model validity against the experimental data produced by Yoshimura and Nakamura (2010a) by setting the model input parameters and run conditions to match those described in their study (Figure 4.9). Following an instantaneous decompression from 100 to 50 MPa at 800°C with 3.2 wt.% starting water and 2.5 hours of equilibration, our produced CO_2 diffusion profiles fit the experimental data remarkably well. One implication of this fit is that bubble nucleation happens relatively instantaneously after decompression, as the model would suggest that the bubbles equilibrate for the full 2.5 hours. One disagreement between the model and

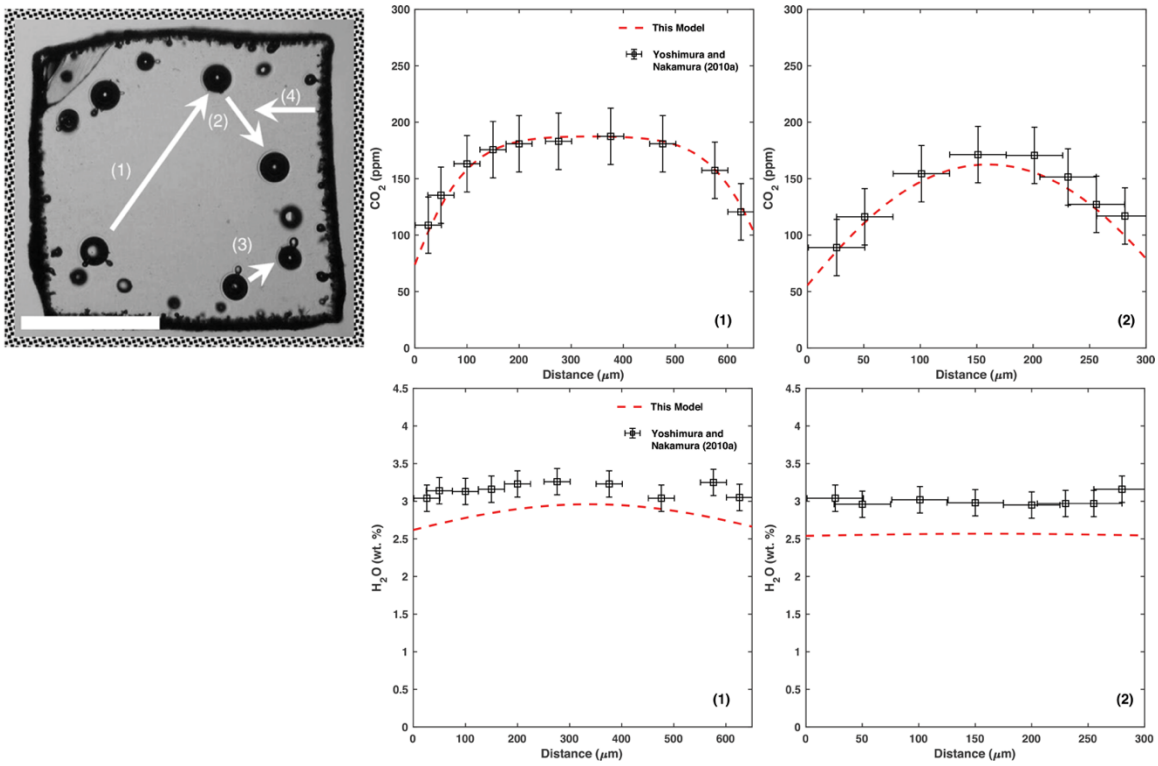

Figure 4.9. Model tested against decompression experiments of Yoshimura and Nakamura (2010a). Top left, a picture of the experimental product with differently spaced but evenly sized bubbles is shown with transects labeled. The middle and right columns show the comparison between the experimental data (open squares) and our model output (dashed line) for CO_2 and H_2O concentrations across transects (1) and (2), respectively.

experimental data appears in the H_2O concentrations. The elevated H_2O concentration in the experimental data versus the model could be explained by error in the FTIR measurements and the variability from the calculated equilibrium concentration due to compositional variation of the obsidian from the sample used in the Liu et al. (2005) solubility experiments.

For small pressure-drops (≤ 20 MPa), we witnessed behavior where the largest bubbles equilibrated the most quickly, which is inverted from the results shared above. With small changes in pressure and therefore solubility, the vapor buffering behavior of large bubbles results in less H_2O being transported into the bubble, allowing for higher

diffusivities for CO_2 than for small bubbles who pull more H_2O out of the melt to preserve vapor composition. Additionally, when initial water content is raised sufficiently (3.25 wt.%, for example), the effect of bubble size on equilibration time becomes entirely negligible.

The results of this model demonstrate the importance of the melt-shell thickness on bubble equilibration and growth timescales. While this model did not take deformation into account, in a natural system, bubbles that grow significantly and reduce the distance between themselves and neighboring bubbles will equilibrate exponentially faster, as the length between bubbles that volatiles must be transported across shrinks. Additionally, the length between bubbles can be used as a proxy for bubble number density with the simple conversion:

$$BND \approx \frac{10^{18}}{L^3}$$

where BND is bubbles per m^{-3} and L is length between bubble centers in microns. At higher bubble number densities, the volatile diffusion length decreases, lowering equilibration time and increasing overall volatile exsolution from the magmatic system (Gardner et al., 2016). Bubble number density and nucleation rates are controlled strongly by the ascent rate, so there is a complicated feedback loop between bubble growth, bubble nucleation, and magma ascent, as faster growth rates result in highly dynamic bulk melt density (Mourtada-Bonnefoi and Laporte, 2004; Toramaru, 2006).

The primary result of this study is shown in Figure 4.8 where regimes of equilibrium and non-equilibrium degassing are parameterized by bubble-spacing (and

BND by proxy) and decompression rate. This figure shows the beginnings of the development of a clear framework for determining degassing style and relative importance of diffusive limitation based on simplified parameters. One can easily imagine how a system may evolve across the diagram and change degassing styles as magmas speed or slow their ascent and nucleate or resorb bubbles. The validity of this framework is further reinforced by the agreement of the slope of the dashed gray lined in the second panel of Figure 4.8 with the scaling relationship proposed by Gonnerman and Manga (2005b) that says the BND for which degassing style transitions from equilibrium to nonequilibrium degassing should scale with $(dP/dt)^{3/2}$. The ability to quickly and accurately simplify individual bubble behaviors into simple parameters will be invaluable to conduit models seeking to explore the complex interplay of factors that control bubble growth and resorption.

CHAPTER V

EXPERIMENTAL RESULTS AND DISCUSSION

5.1 Solubility Experiment Results

To best model decompression experiments, the starting melt should be saturated with volatiles and in equilibrium with the surrounding fluid for that specific pressure and temperature conditions. In order to ensure volatile saturation was achieved, we performed a series of solubility experiments where capsules containing natural Mono Craters obsidian were held at 800°C and 100 MPa for varying durations and quenched before decompression. To determine the time required to reach equilibrium solubility, we held capsules at this pressure and temperature for 4, 6, and 8 days. The results of these experiments are presented in Figure 5.1 and Table 5.1. Variations in the H_2O–CO_2 fluid and dissolved volatile composition are a result of variability in the OAD, NNO, and glass chemistry. Between 4 and 8 days spent equilibrating, the standard deviation of CO_2 concentrations shrank from 68 ppm to 13 ppm. Over the same time period, the standard deviation of H_2O concentration values dropped from 0.15 wt.% to 0.07 wt.%. The equilibrium variability of dissolved volatile concentration depends on the accuracy of the measurements as well as compositional variability in natural samples. The uncertainty of

Table 5.1. List of solubility experiments. Mean concentrations presented with 2σ uncertainty

Experiment #	Temperature (°C)	Pressure (MPa)	Equilibration time (days)	$[H_2O]_f$ (wt.%)	$[CO_2]_f$ (ppm)
b5	800	100	4	2.42±0.30	292±136
b6	800	100	6	1.95±0.27	348±77
b7	800	100	8	2.83±0.14	358±25
b20	800	100	25	4.531±0.27	n/a
b24	800	100	13	4.27±1.14	n/a

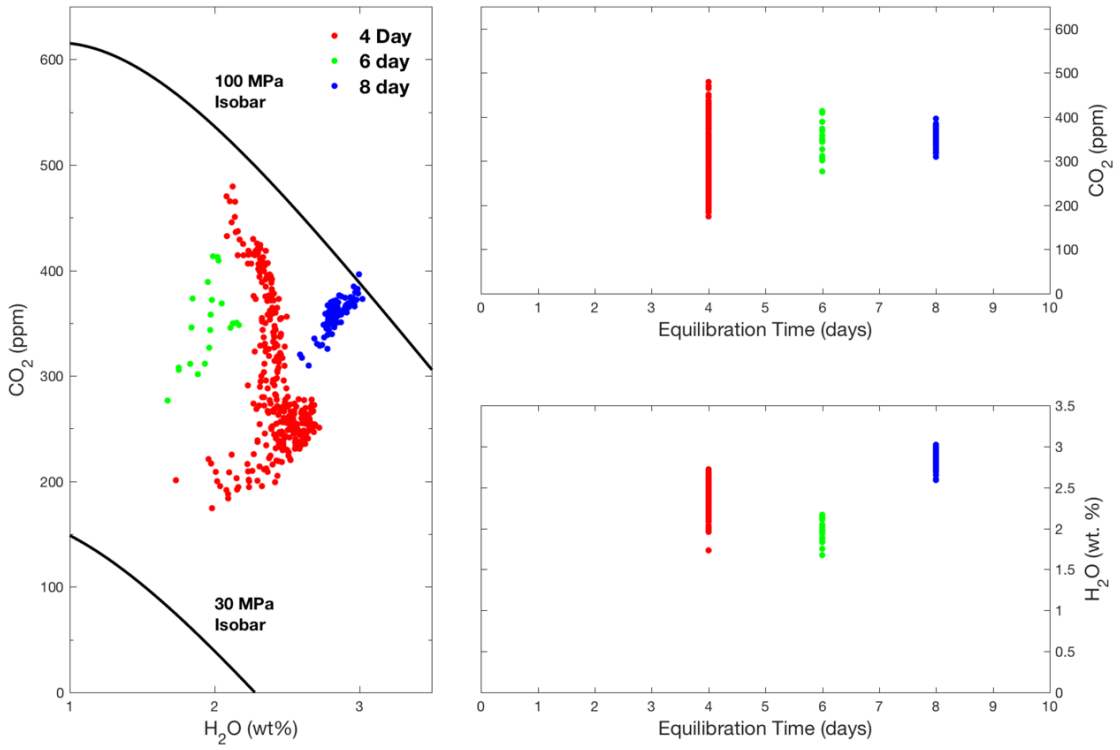

Figure 5.1. *Left Panel* H_2O–CO_2 concentration in glass, as measured by FTIR, after 4, 6, and 8 days. As equilibration duration increases, the spread in CO_2 shrinks and approaches the isobar concentration. Isobars drawn from Liu et al. (2005) solubility relationship.
Right Panels The same CO_2 (upper) and H_2O (lower) concentrations plotted over time to demonstrate lessening variability as glass approaches equilibrium saturation.

H_2O concentration in silicate glasses as measured by FTIR is 0.05 wt.% (Devine et al., 1995). From these results, we took 8 days to be the minimum amount of time required to fully saturate a 2 mm diameter cylinder surrounded by volatile rich fluid with H_2O and CO_2.

We performed two additional solubility experiments whose results can be seen in Table 5.1. In both of these experiments, the capsule exchanged fluid with the H_2O pressure medium, and CO_2 was lost. Experiment b20 (Figure 5.2) equilibrated a sample of synthetic obsidian for 25 days before quenching. The resulting glass was homogeneous

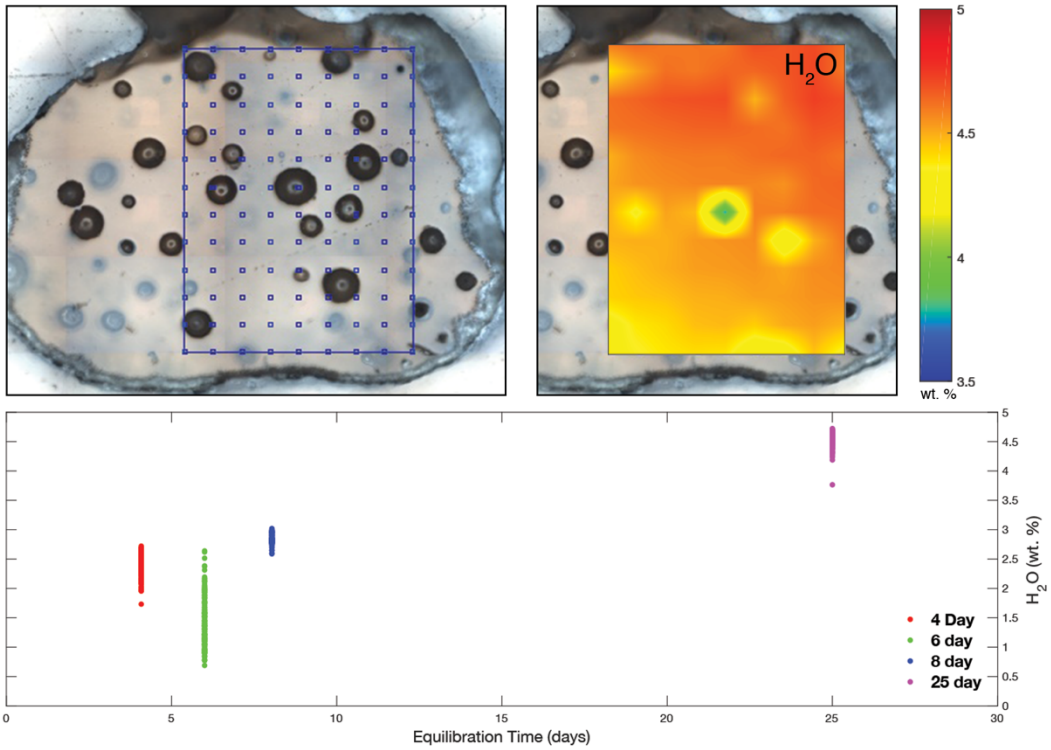

Figure 5.2. Synthetic obsidian equilibrated at 800°C and 100 MPa for 25 days. Interior of capsule did not remain isolated from H_2O pressure medium causing CO_2 to be lost from the glass. The concentration map in the top-right shows the homogeneity of H_2O concentration across the glass. The large bubble in the center of the sample causes the apparent heterogeneity. The bottom plot shows H_2O concentration over time. Variability in H_2O concentration doesn't change between 8 days and 25 days.

within measurement uncertainty with one outlier, which can be ascribed to an analytical artifact caused by a large bubble that deflated absorbance through thinning and/or scattered the beam.

Figure 5.3 shows the results of experiment b24 in which a cylinder of natural obsidian with abundant texture and microlites was equilibrated for 13 days in order to explore the effects of texture on both the solubility relationship as well as the FTIR measurements. In both cases, the texture was found to have minimal effect on solubility and diffusion as well as on the FTIR analysis.

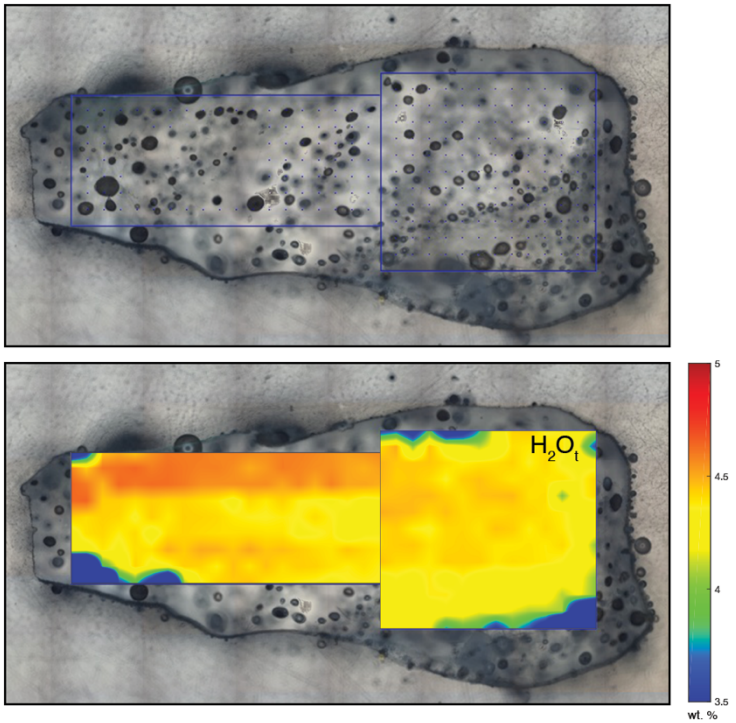

Figure 5.3. Mono Craters obsidian with abundant vesicles equilibrated at 800°C and 100 MPa for 13 days. Interior of capsule did not remain isolated from H_2O pressure medium causing CO_2 to be lost from the sample. Lower panel shows map of H_2O concentration across sample.

5.2 Mixed Volatile Decompression Experiment Results

In order to expand the body of mixed-volatile (H_2O–CO_2) continuous decompression experiments, 17 experimental runs were attempted, and the results of those that were analyzed are presented in Table 5.2. Of the experiments attempted, two capsules with synthetic obsidian remained closed systems and had measureable CO_2 in addition to H_2O. One sample, equilibrated for 15 days before decompression, displayed no bubbles after being decompressed (Figure 5.4). Two lateral slices were made through

Table 5.2. List of mixed-volatile decompression experiments. Mean concentrations presented with 2σ uncertainty

Experiment #	Temperature (°C)	Initial Pressure (MPa)	Final Pressure (MPa)	Equilibration time (days)	dP/dt (MPa/s)	$[H_2O]_f$ (wt.%)	$[CO_2]_f$ (ppm)
b11	800	100	30	15	0.01	1.05±0.30	488±94
b26	800	100	30	25	0.01	1.84±0.16	495±84

this capsule to be polished and analyzed by FTIR following decompression and quenching. Both slices display spatial heterogeneity in their dissolved H_2O and CO_2 concentrations. The H_2O concentrations of the upper slice (Slice 1) have a negative correlation with the CO_2 concentrations with H_2O content decreasing towards the bottom-left of the sample and CO_2 content increasing. The lower slice (Slice 2) shows much less

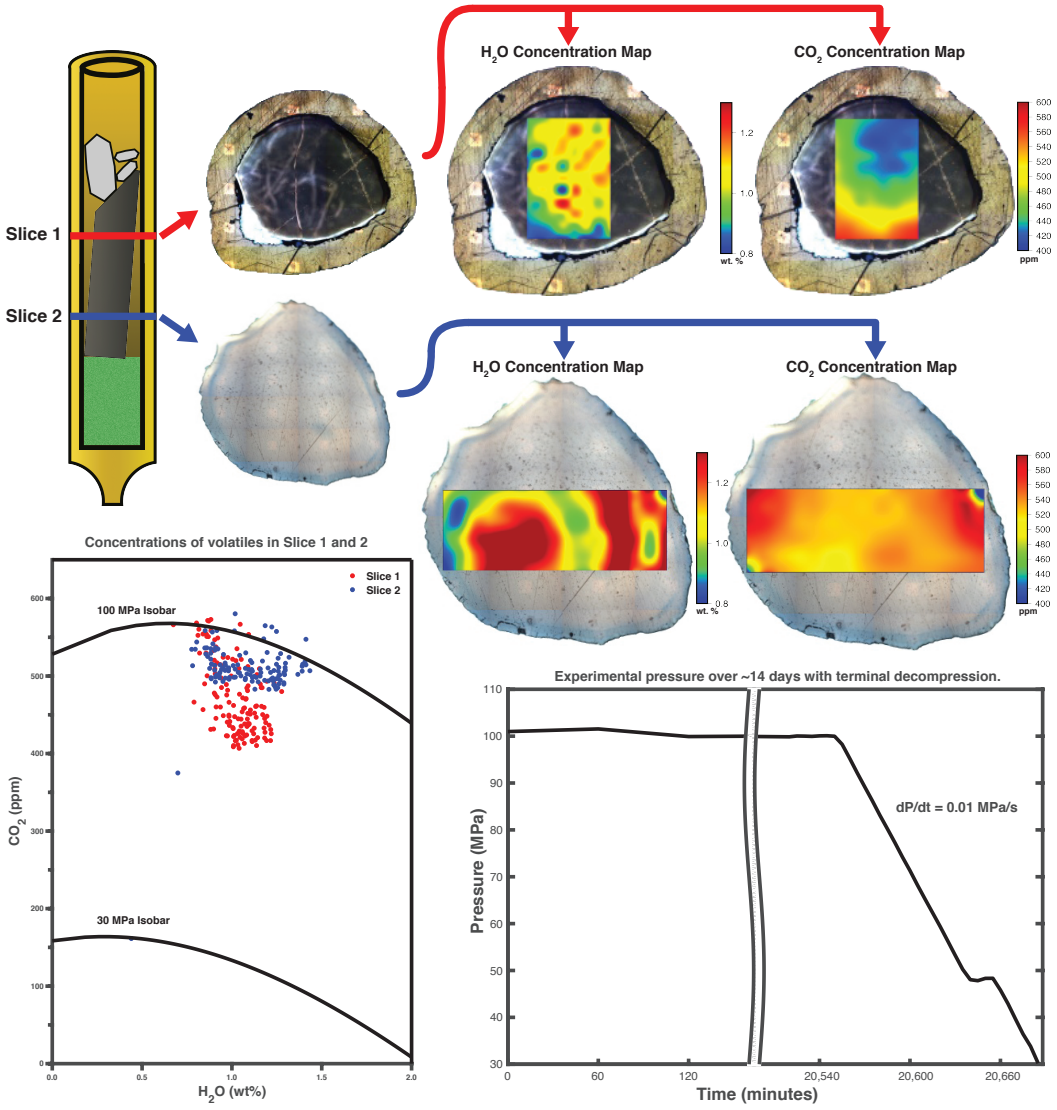

Figure 5.4. Synthetic obsidian equilibrated at 800°C and 100 MPa for 14 days and decompressed to 30 MPa at 0.01 MPa/s. Two cross-sections were taken from different ends of the sample and analyzed as shown in the upper right panels. The bottom-left panel shows CO_2 and H_2O concentrations plotted with 100 and 30 MPa isobars as shown with the solid, black lines. The bottom-right panel shows the decompression path.

variability in the CO_2 content across the sample, but H_2O concentrations display a striking concentric variation with multiple rings of high and low H_2O content. No bubbles were found in this sample. While the surrounding capsule was lost during the preparation of Slice 2, Slice 1 retains its gold ring, which suggests that the fluid may not have been flowing freely around the entire sample and may have been confined to the gap in the lower left.

In one sample, CO_2 was preserved, and bubbles nucleated homogenously as presented in Figure 5.5. In the far-field melt of the sample, H_2O concentrations remained consistent with little variability with the edges of the area map recording a small depletion in H_2O content. CO_2 concentrations displayed greater spatial variability with lower concentrations in the center of the sample and CO_2 contents increasing outwards. The depletions in H_2O and CO_2 in the center right of the sample are localized around a

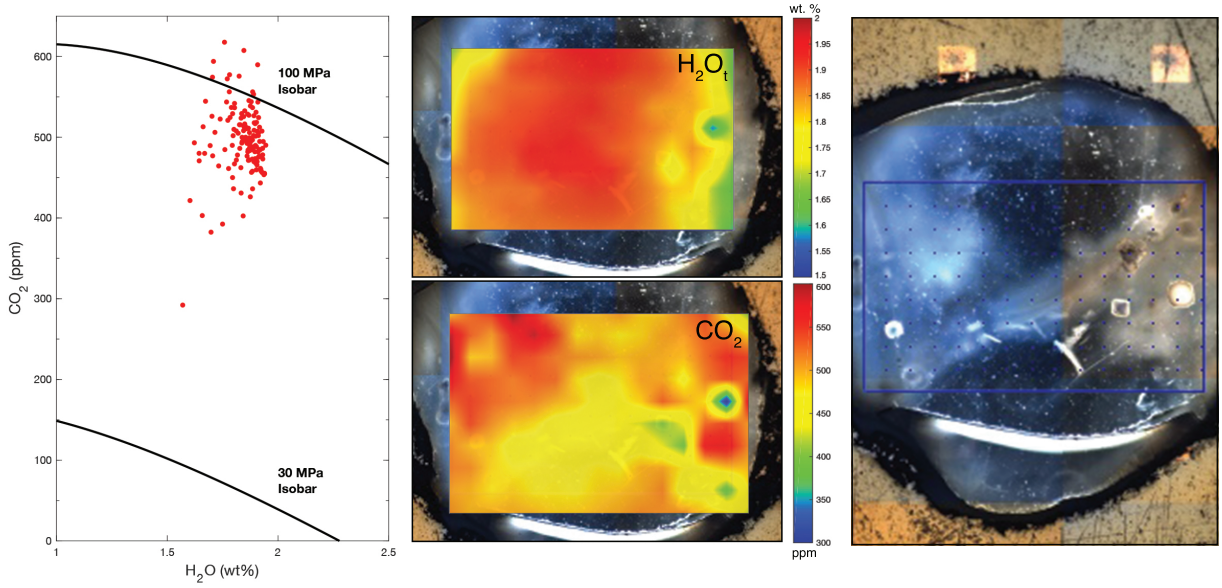

Figure 5.5. Synthetic obsidian sample equilibrated for 25 days then decompressed at 0.01 MPa/s from 100 to 30 MPa. Left panel shows CO_2 and H_2O concentrations plotted with 100 and 30 MPa isobars as shown with the solid, black lines. Middle panels display spatial variability of H_2O and CO_2 concentrations. Right panel shows texture of sample with bubbles appearing in white.

bubble, but it isn't clear whether this depletion is a real feature, an artifact of the bubble affecting the FTIR analysis, or a combination of the two.

5.3 H_2O Only Experiment Results

Capsules that did not remained isolated from the pressure medium lost CO_2 but were still fully saturated with H_2O at the time of decompression. One such experiment decompressed a sample of natural obsidian, forming abundant vesicles (Figure 5.6). Spot analyses of H_2O concentrations were taken where remaining melt shells between bubbles were sufficiently thick to allow for FTIR analysis. Variations in color visible in banding surrounding bubbles suggests spatial concentration gradients that could be resolved through further analysis using a higher resolution analytical technique such as synchrotron-FTIR or ATR spectroscopy.

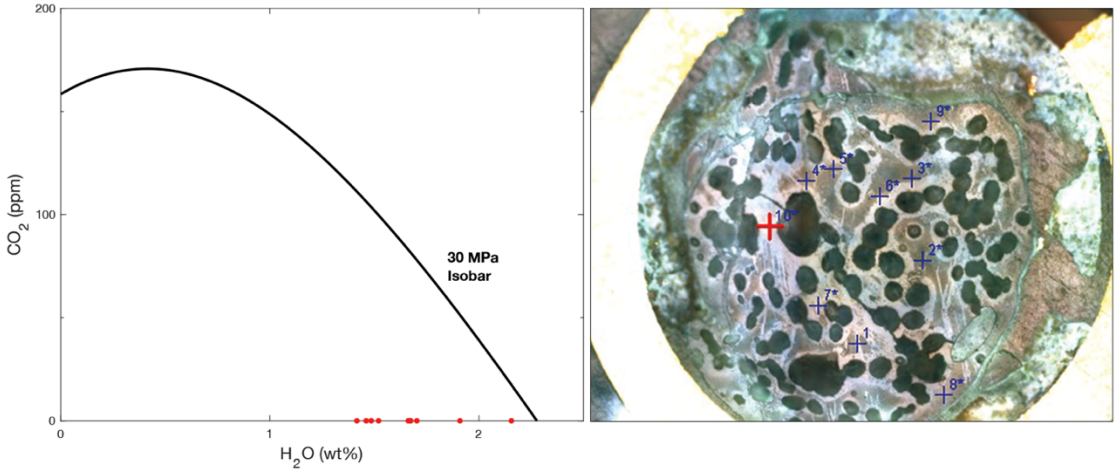

Figure 5.6. Natural obsidian equilibrated at 800°C and 100 MPa for 11 days and then decompressed to 30 MPa at 0.01 MPa/s. Interior of capsule did not remain isolated from H_2O pressure medium causing CO_2 to be lost from the sample, as shown in the left panel with the red points displaying H_2O concentrations at the point analyses shown on the right.

5.4 Discussion of Experimental Results

Robust experimental results for bubble dynamics and degassing processes are necessary for improving the fields of conduit and eruption dynamic modeling. The step-decompression experiments of Yoshimura and Nakamura (2010a) laid a fundamental foundation for modeling nonequilibrium growth and resorption of bubbles in a multivolatile magmatic system. This study was motivated by a need to expand on this previous work by performing mixed-volatile H_2O–CO_2 continuous decompression experiments with decompression rates ≤0.01 MPa/s.

Initial experiments of this type that used natural obsidian as their sample material proved promising but were variable in their nucleation style with one experiment presenting bands of small bubbles and another experiment—identical except in natural variability of obsidian—degassing entirely into one large bubble (Figure 5.7). Due to the unpredictable behavior of bubble formation when using natural obsidian with pre-existing vesicles, microlites, and other impurities, we began loading our capsules with the

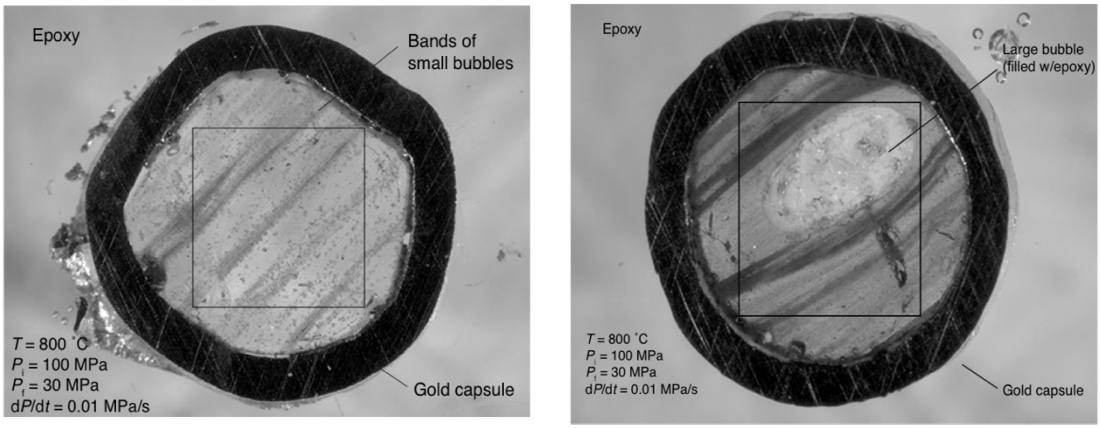

Figure 5.7. Two natural obsidian samples equilibrated at 800°C and 100 MPa for 4 days each and subsequently decompressed to 30 MPa at 0.01 MPa/s. Left image shows bands of small bubbles dominating degassing. Right image shows the large bubble that dominated degassing. No difference between samples or experimental procedure except natural variation in obsidian.

synthetic obsidian described in Chapter 2.1 in an attempt to force the system from heterogeneous to homogenous nucleation of bubbles. In our decompression experiments though, we had difficulty achieving the critical overpressure needed to initiate homogeneous nucleation in these impurity-free obsidians and did not form vesicles as predicted. In a review of decompression experiments, Fiege and Cichy (2015) give a critical supersaturation pressure (ΔP_N) of $>$120-150 MPa required to initiate homogeneous nucleation. While one instance of homogeneous nucleation occurring in our experiments was documented (Figure 5.5), the 70 MPa underpressure may not have been enough to consistently overcome the activation energy needed to nucleate bubbles homogeneously. Experiments with higher underpressures were performed (decompressing from 150 MPa to 30 MPa), but these higher starting pressures were difficult to sustain for sufficient equilibration time without pressure leaks, and no successful experiments were recovered. In future experiments, homogeneous nucleation can be encouraged by increasing the initial equilibration pressure, temperature, and mole-fraction of H_2O in the fluid mixture as predicted by the bubble nucleation kinetics study of Mourtada-Bonnefoit and Laporte (2003).

Even once nucleation is achieved, a balance must then be struck to find the proper nucleation rate for these experiments. If too many bubbles nucleate, two problems will be faced. As can be seen in Figure 5.6, the more bubbles that nucleate and grow, the less melt is present to be measured. Ideally, bubbles of roughly equal sizes would be distributed heterogeneously to explore the effect of diffusion length on vapor–melt equilibration time, as were created in the experiments of Yoshimura and Nakamura

(2010) (Figure 4.9). Additionally, if bubbles are spaced too closely together, the equilibration time can become negligible, and the system will cross into the equilibrium degassing regime. We manage nucleation rate by decompressing at rates (≤0.01 MPa/s) an order of magnitude slower than comparable studies. The bubbles present in Figure 5.5 show promising results for future mixed-volatile experiments using these decompression rates.

Another difficulty faced in the experimental process was preserving the mixed volatile fluid mixture and keeping the interior of the capsules isolated from the H_2O pressure medium. Initially, a thin-walled gold tubing was used in capsule construction, but these capsules could not maintain their integrity through the pressure differentials of pressurization, OAD decomposition, and decompression. The thick-walled gold capsules described in Chapter 2.1 suffer far fewer problems in preserving the closed system but at increased expense. These capsules must also be annealed for at least 3 hours at 1000°C in order to heal micro-fractures, and visual inspection of the micro-welds is vital to ensuring that leaks do not occur.

Two of the eighteen decompression experiments attempted remained closed systems with detectable dissolved CO_2 concentrations. The resulting concentration maps did not display the expected diffusion profiles like those found in Yoshimura and Nakamura (2010a). For the upper slice of sample b11 (Figure 5.4), H_2O and CO_2 concentrations show inverse correlation developing unidirectionally across the sample. One explanation for this behavior is that the apparent fluid pocket between the obsidian

and gold wall was the sole vapor–melt interface around the circumference of the melt with the pressure deforming the gold capsule against the sample and preventing fluid transport. The CO_2 profile—with the highest concentration next to the pocket and lowest at the furthest point away—is then explained by the sample not being fully equilibrated at the time of decompression, despite spending 14 days at pressure and temperature. The inverse profile of the H_2O concentration can then be explained by H_2O having been fully equilibrated and then diffusing out of the melt into the vapor-pocket during decompression.

A similar trend was observed in experiment b26 (Figure 5.5) wherein the CO_2 concentrations were lowest in the center and highest towards the edges, and the H_2O concentrations were fairly homogeneous across the center of the sample but tapered off towards the edges. The depressed CO_2 concentrations in the center can again be attributed to incomplete equilibration—in spite of 25 days of equilibration time. As illustrated by Figure 4.3, equilibration time increases with the length over which volatiles are diffusing squared. Post-hoc numerical modeling of the timescales of volatile dissolution and equilibration shows that for the slab diameters and water contents, more than 50 days would have been required to fully equilibrate the samples if diffusion was occurring around the entire interface and several times longer if diffusion is unidirectional (Figure 5.8). Comparing our experiments to the experiments of Yoshimura and Nakamura (2010a), the difference of a fraction of a millimeter in obsidian slab diameter and 2 wt. % H_2O change the equilibration time from 96 hours to more than 50 days.

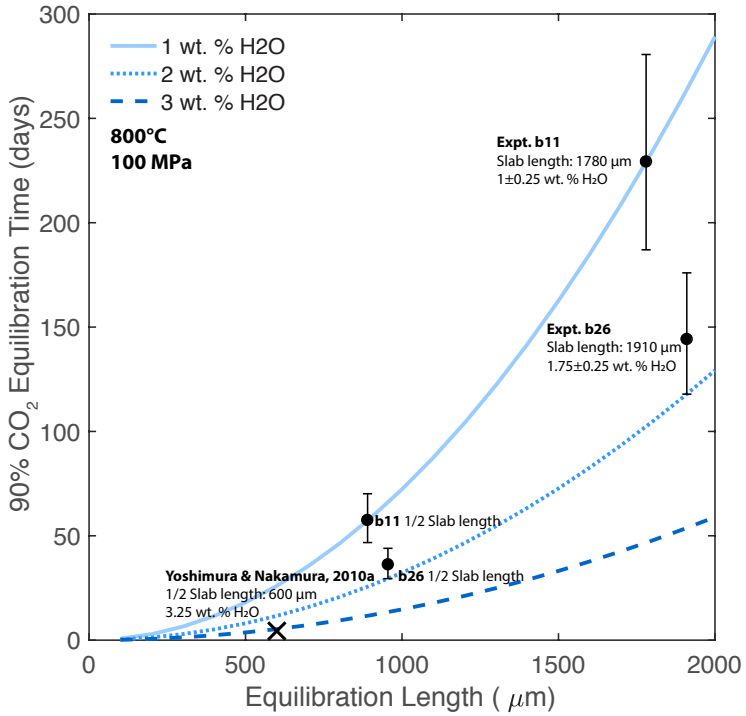

Figure 5.8. Time for CO_2 concentration in the far-field melt to reach 90% of the equilibrium solubility plotted vs. the length over which the CO_2 must dissolve. Different curves represent different wt.% H_2O dissolved in the melt. Experiments are plotted with unidirectional diffusion distances and half-slab lengths. For comparison, the half-slab length equilibration time for Yoshimura and Nakamura (2010a) is plotted.

At the time of writing, the next generation of experiments is being undertaken as informed by the discussion above. To ensure full equilibration, the obsidian slab is replaced by sieved ash with ~50 µm grain size. In addition to reducing the diffusion length and providing for greater fluid pathways, the voids between ash particles trap gas during sintering, which eliminates the need for nucleation to occur. While beneficial for studying growth dynamics, eliminating nucleation from the system diminishes the usefulness of the experiment for studying bubble nucleation dynamics. Additionally, we are modifying the volatile fluid composition by adding H_2O in addition to the OAD during capsule assembly, which will reduce the overall CO_2/H_2O concentration ratio, better representing real magmatic systems.

One of the simplifying assumptions made in the diffusion models is that the melt immediately adjacent to the vapor, whether it is in a bubble or otherwise, remains in equilibrium with the vapor based on the current solubility conditions. The CO_2 vs. H_2O concentration plots for all experiments, however, are not consistent with this vapor–melt equilibrium assumption, as the range of dissolved volatile concentrations should display a complete spread of values between the 30 and 100 MPa isobars. As we don't take the time of diffusion across the vapor–melt interface into account, we can therefore consider any timescales of equilibration to be minimum values calculated under the assumption of vapor–melt equilibrium.

CHAPTER VI

CONCLUSION

This study contributes to a growing body of work examining the complicated interplay of factors that influence the equilibration times of vapor and melt in volcanic systems. Our modeling results quantify the first-order control of bubble spacing on the equilibration time as well as the influence of other variables such as bubble size, magnitude of pressure drop, temperature, and decompression rate. The evolution of bubble spacing depends on bubble nucleation and growth rates as well as their relative motion to each other, so further studies into nucleation and vapor–melt dynamics will be vital to the continued development of conduit models. The results from experiments herein inform future experimental work and further stress the importance of being mindful of the effect of diffusion distance and fluid pathways on equilibration time not only in experimental design but also when thinking about magmatic systems.

The results of the numerical modeling performed by this study provide an initial framework for quickly assessing the sensitivity of equilibration time to different variables as well as determining degassing regime based on a few, simplified parameters. Many conduit models work under the assumption of equilibrium degassing, but as volatile gradients measured in pyroclasts demonstrate, this assumption may not hold up in reality. The question of equilibrium versus nonequilibrium is important to consider when interpreting the composition of dissolved volatiles in volcanic glass (Rust et al., 2004; Gonnerman and Manga, 2005b; Watkins et al. 2012) or the composition of volcanic gas

emissions (e.g., CO_2/S, H_2O, CO_2, etc.; Burton et al., 2000; Duffell et al., 2003; Aiuppa et al., 2007). This study represents a step forward in defining chemical equilibrium, articulating the difference between chemical and physical re-equilibration, and quantifying the factors that influence re-equilibration rates. The principles of vapor-melt re-equilibration in response to a temperature or pressure perturbation can be of use to volcanologists who deal with volatiles including those who analyze gas-monitoring measurements, conduit modelers seeking to examine the response of bubbly fluids to seismic waves of different frequencies (e.g., Karlstrom and Dunham, 2016), and those who wish to better understand bubble nucleation, growth, and the complex interplay of it all with magma ascent.

APPENDIX A

TABLE OF EXPERIMENTS PERFORMED

Expt. #	Experiment Type	Temp (°C)	P_{eq} (Mpa)	t_{eq} (days)	P_f (Mpa)	dP/dt (Mpa/s)	Glass Material	Weigh same before/after?
Bubbles_5	Solubility	800	100	4	100		Mono Craters	Y
Bubbles_6	Solubility	800	100	6	100		Mono Craters	Y
Bubbles_7	Solubility	800	100	8	100		Mono Craters	Y
Bubbles_8	Decompression	800	100	11	30	0.01	Mono Craters	N
Bubbles_9	Decompression	800	100		30	0.01	Mono Craters	N
Bubbles_10	Decompression	800	100	6	30	~0.12	Synthetic	N
Bubbles_11	Decompression	800	100	15	30	0.01	Synthetic	Y
Bubbles_12	Decompression	800	100	20	30	0.1	Synthetic	Y
Bubbles_13	Decompression	800	100	11	30	0.01	Synthetic	Y
Bubbles_14	Decompression	800	100	7	30	0.01	Synthetic	Y
Bubbles_15	Decompression	800	100	14	30	0.01	Synthetic	Y
Bubbles_16	Decompression	800	100	10	30	0.01	Synthetic	N
Bubbles_17	Decompression	800	100	9	30	0.01	Synthetic	N
Bubbles_18	Decompression	800	100	4	30	0.01	Synthetic	N
Bubbles_19	Decompression	800	100	8	30	0.025	Synthetic	N
Bubbles_20	Solubility	800	100	25	100		Synthetic	N
Bubbles_21	Decompression	800	100	8	20	0.001	Synthetic	N
Bubbles_22	Decompression	800	150	14	30	0.03	Synthetic	N
Bubbles_23	Decompression	800	100	14	20	0.001	Synthetic	N
Bubbles_24	Solubility	800	100	13	100		Natural w/ texture	N
Bubbles_25	Decompression	800	100	14	41	0.01	Synthetic	N
Bubbles_26	Decompression	800	100	25	30	0.01	Synthetic	Y

APPENDIX B

SHARDS OF FIRE

This is a popular science article written for ComSciCon-PNW 2017 and intended for publication.

Shards of Fire:
The Mysterious Origins of Volcanic Glass

Fountains of lava, pyroclastic flows, and ash clouds climbing high in the atmosphere—all wrapped in an element of danger— make for charismatic science. The appeal of volcanoes is so widespread that they have even found their way into our homes: look in the rock collection of any child, and nestled between the rose quartz and fool's gold, you'll probably find obsidian.

This glassy, volcanic rock has fascinated humans for millennia as much for its beauty as for its usefulness in arrowheads. At first glance, the origin of obsidian appears simple, as lava cools quickly enough that crystals can't form. However, the lustrous, black depths of these enigmatic rocks hold mysteries about their formation that continue to puzzle earth scientists today.

The appearance of obsidian depends on the absence of water. It may seem natural that molten rock ten times hotter than water's boiling temperature would be free of water. At the depths and pressures from which magma comes though, water is perfectly happy to coexist with and remain dissolved in the molten rock. Amazingly, a gallon of magma deep underground can contain up to two cups of water. However, the lavas from obsidian flows that form dome-shaped hills lose almost all of their water before cooling to glass. This happens as water naturally separates from the magma during its rise from deep chambers to the surface, but removing the bubbles that form while creating obsidian's signature smooth texture proves to be a troublesome process.

When magma ascends to the surface and depressurizes, bubbles begin to form as water boils out of the molten rock. These bubbles then increase magma buoyancy, which speeds the magma's rise to the surface. In cases of runaway bubble formation, the accelerating magma will explosively become a foam and eventually be ejected at high speeds out of the volcano as ash and pumice, a highly bubbly rock. Though seemingly opposites in appearance, pumice and obsidian have identical sources; however, the obsidian somehow was able to lose the majority of its bubbles before freezing while the molten rock was still liquid while the pumice was not.

Waiting for the foam to settle on a hastily poured beverage can sometimes feel like an eternity, but foamy magmas require even more time for the bubbles to leave a lava, taking months or longer. The stickiness of molten rock keeps the bubbles from rising out easily. For reference, the average obsidian lava is about a million times more viscous than honey—and up to one-hundred billion times depending on the temperature, water, and crystal content. This is a similar viscosity to the famous "pitch drop" experiments—a funnel of liquid tar that drips only about once a decade. Complicating matters more, the lava must remain hot enough to stay molten and not freeze into glass for the period that bubbles are slowly escaping the foam.

How then can the obsidian stay molten long enough for the foam to collapse? At volcanoes with massive obsidian flows, slow moving rivers of fire flows make hill-sized domes on the surface during oozing, relatively peaceful eruptions. Hot and insulating lava erupted before and after the future-obsidian can then sandwich the bubbly layer acting as a blanket, holding the heat in and keeping the obsidian liquid.

Adding to the puzzlement of volcanologists, chips of volcanic glass in ash beds, far from these thick, layered flows can be found by visitors to many volcanic systems like Mono-Inyo Craters in California, Newberry Caldera in Oregon, and Yellowstone Caldera in Wyoming . These chips, or obsidian pyroclasts—Greek for "shards of fire"—can't have been kept hot enough for months in their ash beds. Instead, they must have formed underground, in the heart of the volcano, and been ejected with the pumice and ash during an explosive eruption.

Observations of obsidian pyroclasts reveal several mysterious differences from obsidian flows. First, these quarter sized bits of pyroclastic glass manage to retain much of their water, up to 25 times as much water as in flows, and their water content can vary greatly from one side of a chip to the other. Second, the pyroclasts preserve complicated starburst-shaped bubbles that cannot be explained through the foam settling process called upon to explain obsidian flows.

To address these complications and improve understanding of the fiery inner workings of volcanoes, scientists have developed a new mechanism to explain the formation of obsidian during explosive eruptions. Rather than having the entire magma foam up as a whole and then lose its bubbles during and after an effusive eruption, scientists suggest that pyroclast forming magmas do fragment and explode, temporarily becoming pumice and ash rather than a cohesive lava flow.

Before these fragmental bits of molten rock can be rocketed to the surface though, some may stick to the inner walls of the volcano. This accumulation of hot ash and pumice can then stay stuck long enough to heal back into a cohesive mass like squishing together bits of hot wax. The gas trapped between these sharp fragments of ash then forms the previously unexplainable starburst bubble shapes, solving the first part of the mystery.

Having the obsidian form underground rather than at the surface also explains how it retains water: the higher pressures keep water in the magma right up until the shards get ripped off the inner wall of the volcano and flash freeze during eruption. The water variability in each pyroclast would also be expected to smooth out over time, so scientists cleverly use the diverse water contents across chips to estimate the time between ash sticking to the wall and pyroclasts being erupted. Before this new mechanism was developed, thousands of hours would have been required to explain the formation of these pyroclasts, but this new method can make smooth glass out of hydrated magma in less than a day.

We've taken a brief look into the origins of this beautiful rock, but many mysteries remain from the small—how do snowflake, mahogany, and rainbow obsidian form? — to the fundamental—what triggers volcanic eruptions, why do they stop, and can we predict them? Volcanoes are complex and chaotic systems, and scientific studies of obsidian tell more than just interesting stories about an attractive rock. The investigation of these pyroclasts has given us a rare, direct look into the processes happening inside of the volcano before, during, and after eruptions.

REFERENCES CITED

Aiuppa, A., Federico, C., Giudice, G., Giuffrida, G., Guida, R., Gurrieri, S., Liuzzo, M., Moretti, R., and Papale, P., 2009, The 2007 eruption of Stromboli volcano: Insights from real-time measurement of the volcanic gas plume CO2/SO2 ratio: Journal of Volcanology and Geothermal Research, v. 182, p. 221–230, doi: 10.1016/j.jvolgeores.2008.09.013.

Aster, E.M., Wallace, P.J., Moore, L.R., Watkins, J., Gazel, E., and Bodnar, R.J., 2016, Reconstructing CO2 concentrations in basaltic melt inclusions using Raman analysis of vapor bubbles: Journal of Volcanology and Geothermal Research, v. 323, p. 148–162, doi: 10.1016/j.jvolgeores.2016.04.028.

Von Aulock, F.W., Kennedy, B.M., Schipper, C.I., Castro, J.M., E. Martin, D., Oze, C., Watkins, J.M., Wallace, P.J., Puskar, L., Bégué, F., Nichols, A.R.L., and Tuffen, H., 2014, Advances in Fourier transform infrared spectroscopy of natural glasses: From sample preparation to data analysis: Lithos, v. 206-207, p. 52–64, doi: 10.1016/j.lithos.2014.07.017.

Becerril, L., Galindo, I., Gudmundsson, A., and Morales, J.M., 2013, Depth of origin of magma in eruptions: Scientific Reports, v. 3, doi: 10.1038/srep02762.

Behrens, H., Tamic, N., and Holtz, F., 2004, Determination of the molar absorption coefficient for the infrared absorption band of CO_2 in rhyolitic glasses: American Mineralogist, v. 89, p. 301–306, doi: 10.2138/am-2004-2-307.

Burgisser, A., and Gardner, J.E., 2004, Experimental constraints on degassing and permeability in volcanic conduit flow: Bulletin of Volcanology, v. 67, p. 42–56, doi: 10.1007/s00445-004-0359-5.

Burton, M.R., Oppenheimer, C., Horrocks, L.A., and Francis, P.W., 2000, Remote sensing of CO2 and H2O emission rates from Masaya volcano, Nicaragua: Geology, v. 28, p. 915, doi: 10.1130/0091-7613(2000)28<915:RSOCAH>2.0.CO;2.

Carmichael, I.S.E., 1966, The iron-titanium oxides of salic volcanic rocks and their associated ferromagnesian silicates: Contributions to Mineralogy and Petrology, v. 14, p. 36–64, doi: 10.1007/BF00370985.

Carroll, M.R., and Rutherford, M.J., 1985, Sulfide and sulfate saturation in hydrous silicate melts, *in* Lunar and Planetary Science Conference Proceedings, v. 15, p. 601.

Clemente, B., 2004, The Solubility of Sulphur in Hydrous Rhyolitic Melts: Journal of Petrology, v. 45, p. 2171–2196, doi: 10.1093/petrology/egh052.

Cooley, J.W., and Tukey, J.W., 1965, An algorithm for the machine calculation of complex Fourier series: Mathematics of Computation, v. 19, p. 297–297, doi: 10.1090/S0025-5718-1965-0178586-1.

Devine, J., Gardner, J., Brack, H., Laynet, G., and Rutherford, M., 1995, Comparison of microanalytical methods for estimating H20 contents of silicic volcanic glasses: American Mineralogist, v. 80, p. 319–328.

Duffell, H.J., Oppenheimer, C., Pyle, D.M., Galle, B., McGonigle, A.J.., and Burton, M.R., 2003, Changes in gas composition prior to a minor explosive eruption at Masaya volcano, Nicaragua: Journal of Volcanology and Geothermal Research, v. 126, p. 327–339, doi: 10.1016/S0377-0273(03)00156-2.

Duncan, M.S., and Dasgupta, R., 2015, Pressure and temperature dependence of CO2 solubility in hydrous rhyolitic melt: implications for carbon transfer to mantle source of volcanic arcs via partial melt of subducting crustal lithologies: Contributions to Mineralogy and Petrology, v. 169, doi: 10.1007/s00410-015-1144-5.

Fiege, A., and Cichy, S.B., 2015, Experimental constraints on bubble formation and growth during magma ascent: A review: American Mineralogist, v. 100, p. 2426–2442, doi: 10.2138/am-2015-5296.

Fine, G., and Stolper, E., 1985, The speciation of carbon dioxide in sodium aluminosilicate glasses: Contributions to Mineralogy and Petrology, v. 91, p. 105–121, doi: 10.1007/BF00377759.

Forman, M.L., 1966, Fast Fourier-Transform Technique and Its Application to Fourier Spectroscopy*: Journal of the Optical Society of America, v. 56, p. 978, doi: 10.1364/JOSA.56.000978.

Gardner, J.E., Jackson, B.A., Gonnermann, H., and Soule, S.A., 2016, Rapid ascent and emplacement of basaltic lava during the 2005–06 eruption of the East Pacific Rise at ca. 9°51′N as inferred from CO 2 contents: Earth and Planetary Science Letters, v. 453, p. 152–160, doi: 10.1016/j.epsl.2016.08.007.

Gonnermann, H., and Manga, M., 2005, Nonequilibrium magma degassing: Results from modeling of the ca. 1340 A.D. eruption of Mono Craters, California: Earth and Planetary Science Letters, v. 238, p. 1–16, doi: 10.1016/j.epsl.2005.07.021.

Gonnermann, H.M., and Manga, M., 2007, The Fluid Mechanics Inside a Volcano: Annual Review of Fluid Mechanics, v. 39, p. 321–356, doi: 10.1146/annurev.fluid.39.050905.110207.

Ihinger, P.D., Zhang, Y., and Stolper, E.M., 1999, The speciation of dissolved water in rhyolitic melt: Geochimica et Cosmochimica Acta, v. 63, p. 3567–3578, doi: 10.1016/S0016-7037(99)00277-X.

Johnston, A., and Senkovich, D., 2007, Rapid Quench Cold-Seal Apparatus with Computer-Controlled Pressure and Temperature Cycling, http://adsabs.harvard.edu/abs/2007AGUFM.V31C0605J.

Karlstrom, L., and Dunham, E.M., 2016, Excitation and resonance of acoustic-gravity waves in a column of stratified, bubbly magma: Journal of Fluid Mechanics, v. 797, p. 431–470, doi: 10.1017/jfm.2016.257.

Liu, Y., Zhang, Y., and Behrens, H., 2005, Solubility of H2O in rhyolitic melts at low pressures and a new empirical model for mixed H2O–CO2 solubility in rhyolitic melts: Journal of Volcanology and Geothermal Research, v. 143, p. 219–235, doi: 10.1016/j.jvolgeores.2004.09.019.

Matthews, W., Linnen, R.L., and Guo, Q., 2003, A filler-rod technique for controlling redox conditions in cold-seal pressure vessels: American Mineralogist, v. 88, p. 701–707, doi: 10.2138/am-2003-0424.

Mavrogenes, J.A., and O'Neill, H.S.., 1999, The relative effects of pressure, temperature and oxygen fugacity on the solubility of sulfide in mafic magmas: Geochimica et Cosmochimica Acta, v. 63, p. 1173–1180, doi: 10.1016/S0016-7037(98)00289-0.

Mourtada-Bonnefoi, C.C., and Laporte, D., 2004, Kinetics of bubble nucleation in a rhyolitic melt: an experimental study of the effect of ascent rate: Earth and Planetary Science Letters, v. 218, p. 521–537, doi: 10.1016/S0012-821X(03)00684-8.

Newman, S., Epstein, S., and Stolper, E., 1988, Water, carbon dioxide, and hydrogen isotopes in glasses from the ca. 1340 A.D. eruption of the Mono Craters, California: Constraints on degassing phenomena and initial volatile content: Journal of Volcanology and Geothermal Research, v. 35, p. 75–96, doi: 10.1016/0377-0273(88)90007-8.

Newman, S., Stopler, E., and Epstein, S., 1986, Measurement of water in rhyolitic glasses; calibration of an infrared spectroscopic technique: American Mineralogist, v. 71, p. 1527–1541.

Prousevitch, A.A., Sahagian, D.L., and Anderson, A.T., 1993, Dynamics of diffusive bubble growth in magmas: Isothermal case: Journal of Geophysical Research: Solid Earth, v. 98, p. 22283–22307, doi: 10.1029/93JB02027.

Proussevitch, A.A., and Sahagian, D.L., 1998, Dynamics and energetics of bubble growth in magmas: Analytical formulation and numerical modeling: Journal of Geophysical Research: Solid Earth, v. 103, p. 18223–18251, doi: 10.1029/98JB00906.

Rust, A.C., Cashman, K.V., and Wallace, P.J., 2004, Magma degassing buffered by vapor flow through brecciated conduit margins: Geology, v. 32, p. 349, doi: 10.1130/G20388.2.

Scandone, R., 1996, Factors controlling the temporal evolution of explosive eruptions: Journal of Volcanology and Geothermal Research, v. 72, p. 71–83, doi: 10.1016/0377-0273(95)00086-0.

Shaw, H.R., 1972, Viscosities of magmatic silicate liquids; an empirical method of prediction: American Journal of Science, v. 272, p. 870–893, doi: 10.2475/ajs.272.9.870.

Smith, B.C., 1996, Fundamentals of Fourier transform infrared spectroscopy: Boca Raton, CRC Press, 202 p.

Sparks, R.S.J., 1978, The dynamics of bubble formation and growth in magmas: A review and analysis: Journal of Volcanology and Geothermal Research, v. 3, p. 1–37, doi: 10.1016/0377-0273(78)90002-1.

Stolper, E., 1989, Temperature dependence of the speciation of water in rhyolitic melts and glasses: American Mineralogist, v. 74, p. 1247–1257.

Stolper, E., 1982, Water in silicate glasses: An infrared spectroscopic study: Contributions to Mineralogy and Petrology, v. 81, p. 1–17, doi: 10.1007/BF00371154.

Toramaru, A., 2006, BND (bubble number density) decompression rate meter for explosive volcanic eruptions: Journal of Volcanology and Geothermal Research, v. 154, p. 303–316, doi: 10.1016/j.jvolgeores.2006.03.027.

Villemant, B., and Boudon, G., 1998, Transition from dome-forming to plinian eruptive styles controlled by H2O and Cl degassing: Nature, v. 392, p. 65–69, doi: 10.1038/32144.

Watkins, J.M., Gardner, J.E., and Befus, K.S., 2017, Nonequilibrium degassing, regassing, and vapor fluxing in magmatic feeder systems: Geology, v. 45, p. 183–186, doi: 10.1130/G38501.1.

Watkins, J.M., Manga, M., and DePaolo, D.J., 2012, Bubble geobarometry: A record of pressure changes, degassing, and regassing at Mono Craters, California: Geology, v. 40, p. 699–702, doi: 10.1130/G33027.1.

Westrich, H.R., 1982, Nucleation and growth rates of bubbles in hydrous obsidian.: EOS, v. 63, p. 1136.

Woods, A.W., and Koyaguchi, T., 1994, Transitions between explosive and effusive eruptions of silicic magmas: Nature, v. 370, p. 641–644, doi: 10.1038/370641a0.

Yoshimura, S., and Nakamura, M., 2010, Chemically driven growth and resorption of bubbles in a multivolatile magmatic system: Chemical Geology, v. 276, p. 18–28, doi: 10.1016/j.chemgeo.2010.05.010.

Zhang, Y., 1999, H_2O in rhyolitic glasses and melts: Measurement, speciation, solubility, and diffusion: Reviews of Geophysics, v. 37, p. 493–516, doi: 10.1029/1999RG900012.

Zhang, Y., Belcher, R., Ihinger, P.D., Wang, L., Xu, Z., and Newman, S., 1997, New calibration of infrared measurement of dissolved water in rhyolitic glasses: Geochimica et Cosmochimica Acta, v. 61, p. 3089–3100, doi: 10.1016/S0016-7037(97)00151-8.

Zhang, Y., and Ni, H., 2010, Diffusion of H, C, and O Components in Silicate Melts: Reviews in Mineralogy and Geochemistry, v. 72, p. 171–225, doi: 10.2138/rmg.2010.72.5.

Zhang, Y., Xu, Z., and Behrens, H., 2000, Hydrous species geospeedometer in rhyolite: improved calibration and application: Geochimica et Cosmochimica Acta, v. 64, p. 3347–3355, doi: 10.1016/S0016-7037(00)00424-5.